2025-08-20

# Magnetic Ordering and Dynamics in Assemblies of Magnetite Nanoparticles Throughout the Superparamagnetic Transition

Johnathon Michael Rackham
*Brigham Young University*

# Magnetic Ordering and Dynamics in Assemblies of Magnetite Nanoparticles Throughout the Superparamagnetic Transition

Johnathon Michael Rackham

A dissertation submitted to the faculty of
Brigham Young University
in partial fulfillment of the requirements for the degree of

Doctor of Philosophy

Karine Chesnel, Chair
Richard Sandberg
Mark Transtrum
Branton Campbell
Benjamin Frandsen

Department of Physics and Astronomy

Brigham Young University

ABSTRACT

Magnetic Ordering and Dynamics in Assemblies of Magnetite Nanoparticles Throughout the Superparamagnetic Transition

Johnathon Michael Rackham
Department of Physics and Astronomy, BYU
Doctor of Philosophy

Magnetic nanoparticles are used in nanotechnologies and biomedical applications, such as drug targeting, hyperthermia treatment, MRI contrasting agents, and bio-separation of compound solutions. Magnetite ($Fe_3O_4$) nanoparticles stand to be effective in these roles due to the non-toxic nature of magnetite and its strong magnetization. To this end, a greater understanding of the magnetic behavior of the individual magnetite nanoparticles is needed when a collection of them is used. This research seeks to discover the local magnetic ordering and dynamics of fluctuations of ensembles of magnetite nanoparticles at various stages of the magnetization process, throughout the superparamagnetic blocking transitions, and for various particle sizes. We use x-ray circular dichroism and x-ray resonant magnetic scattering (XRMS), which provides information about the various magnetic orders in the samples. We discuss the modeling of the magnetic scattering data using a one-dimensional chain of nanoparticles in real space as well as an empirical Gaussian packet model in reciprocal space. We find that at low temperature, and field values close to the coercive point, magnetite nanoparticles experience a significant amount of antiferromagnetic ordering which increases with particle size. We present real space magnetic images of the nanoparticles obtained via dichroic x-ray ptychography, which confirm our predictions from scattering. Finally, we investigate the dynamics of magnetic fluctuations by using x-ray photon correlation spectroscopy.

Keywords: [magnetite, nanoparticles, magnetic scattering, XRMS, computational modeling, ptychography, XAS, XMCD, XPCS]

ACKNOWLEDGMENTS

I would like to thank the diligent guidance of my advisory committee, particularly Dr. Karine Chesnel for her service as committee chair and support for many years. Additionally, the support of BYU Physics department, and the bottomless patience of my family and friends which was invaluable. I would not have made it this far without all of you.

This research used additional resources of:

- The National Synchrotron Light Source II, a U.S. Department of Energy (DOE) Office of Science User Facility operated for the DOE Office of Science by Brookhaven National Laboratory under Contract No. DE-SC0012704, and with the assistance of Claudio Mazzoli.
- The Advanced Light Source, a U.S. DOE Office of Science User Facility under contract no. DE-AC02-05CH11231, and with the assistance of Alex Ditter, and David Shapiro.
- Synchrotron SOLEIL for provision of synchrotron radiation facilities and we would like to thank Nicolas Jaouen, and Horia Popescu for assistance in using the Sextants beamline.
- The BYU Microscopy Facility for all the TEM and SEM imaging.

# Contents

# Chapter 1

# Introduction and Background

This research seeks to probe the nanoscale magnetic properties of magnetic nanoparticles. We will probe properties such as the inter-particle correlations, local magnetic ordering, and their associated fluctuation dynamics throughout the superparamagnetic blocking transition by utilizing scattering data collected at synchrotron facilities. In this section, we will discuss the motivation for exploring this topic and what is currently understood about magnetic nanoparticle materials.

## 1.1 Motivation

Magnetic nanoparticles (NPs) are a vital part of many applications in biomedicine and other nanotechnologies [1]. There is a growing interest in NP for drug targeting, MRI, and bio-separation applications [2–4]. For example, contrasting agents, which are chemicals injected into the imaged tissue, are often used in the MRI process to provide a greater ability to differentiate between tissue bodies and types. However, these contrasting agents often pose additional health risks to patients because of their toxicity [5]. Because magnetite ($Fe_3O_4$) NPs are non-toxic, they are excellent candidates for MRI contrast agents in addition to these other applications [6].

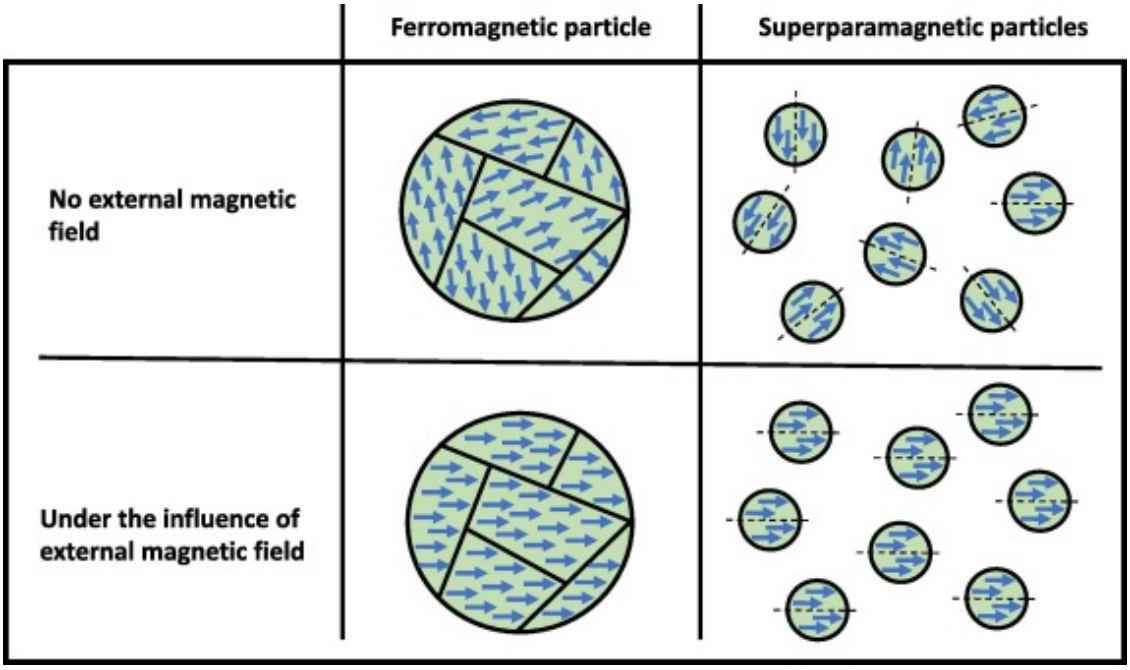


**Figure 1.1** Illustrates the differences between ferromagnetic, and superparamagnetic particle behavior both when exposed to an external magnetic field and with no field present. Figure extracted from here [7].

Magnetite is a ferrimagnetic iron oxide that is commonly occurring and readily found in many minerals. This makes it ideal for use in drug targeting and bio-separation where large quantities of NPs are needed. When certain enzymes are attached to the NPs containing treatment drugs, the functionalize NPs can then be dragged by a magnetic field in the body to specific locations depending on which particular enzymes are used. This could provide a more efficient way to treat cancer as the drugs can be released at the location of the tumor rather than applied globally in a more damaging way. A similar approach to using NPs and enzymes can be used to separate biological components of solutions by allowing the components to bond with the enzyme attached to the NP and then applying an external magnetic field to pull the NPs and targeted components away.

Additionally, magnetite nanoparticles are superparamagnetic and exhibit a thermal blocking temperature. Superparamagnetism is a phenomenon observed in ferromagnetic or ferrimagnetic nanoparticles, where each particle behaves as a single magnetic domain and can be described

as having a nanospin moment on this scale as shown in Fig. 1.1. This behavior occurs because, at such small sizes, the energy barrier that keeps the nanoparticle's magnetic moment aligned in one direction becomes comparable to the thermal energy of the sample. As a result, thermal fluctuations randomly flip the direction of their magnetization. However, when the temperature of the nanoparticle sample cools below a certain point, the blocking temperature ($T_B$), there is no longer enough thermal energy present to cause the particles to flip their nanospin orientations and the ensemble of particles therefore becomes magnetically frozen.

Magnetite's bulk properties have been widely studied [8, 9], but a better understanding of magnetite NPs, rather than bulk material, is needed for the substance to be effective in the applications mentioned above because their technological applications are driven by their nanoscale properties.

## 1.2 Prior Work

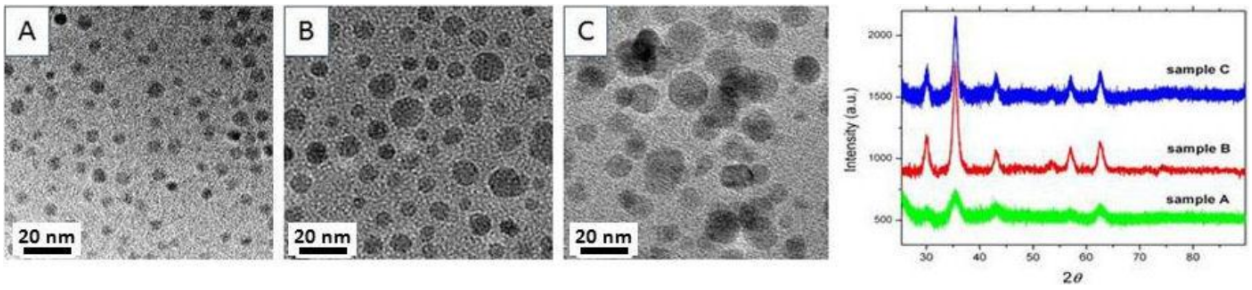


**Figure 1.2** TEM images and XRD patterns of the $Fe_3O_4$ nanoparticles (A) 5 nm (B) 8 nm (C) 11 nm extracted from [10].

Because of this rising interest in magnetite NPs, recent research has focused on the various magnetic properties of these NPs, such as their magnetic response to an external field stimulation, and superparamagnetic blocking transition upon cooling. But most of the current knowledge is based on macroscopic, or ensemble averaged information, and little is known about the magnetic behavior of nanoparticles at the nanoscale. In our group, we are studying the nanoscale magnetic

properties of $Fe_3O_4$ NPs with sizes in the range of 5 to 100 nm [11] using tools such as x-ray magnetic scattering, x-ray ptychography and x-ray correlation spectroscopy to access the missing nanoscale information. Vibrating sample magnetometry (VSM) helps determining the ensemble-average magnetic behavior of these NPs, and allows for the extraction of information regarding their superparamagnetic behavior and blocking temperatures discussed further below.

X-ray magnetic circular dichroism (XMCD) is a spectroscopic technique that measures the difference in x-ray absorption between left and right circularly polarized light in a magnetic material subjected to a magnetic field. XMCD analysis involves recording two X-ray absorption spectra (XAS): one with left and one with right circularly polarized X-rays. The difference between these spectra constitutes the XMCD spectrum and reveals detailed, element-specific information about the magnetic properties of matter, such as spin and orbital magnetic moments.

The XMCD calculations for $Fe_3O_4$ found values of orbital and spin contributions to the magnetic moment that indicated a quenching of the orbital moment and a dominating spin moment that is slightly lower than what is expected in bulk magnetite [12]. X-ray diffraction (XRD) measurements of $Fe_3O_4$ NPs revealed that the crystallographic structure of individual particles is consistent with the crystal structure of bulk magnetite, as shown in Fig. 1.2.

Fig. 1.3 shows a set of field cooling (FC) and zero field cooling (ZFC) measurements which are collected by cooling the sample in the presence of an external field (FC), or without a field presence (ZFC). The magnetization is then tracked as the sample increases in temperature again. The FC-ZFC curves shown in Fig. 1.3 all indicate a superparamagnetic behavior at high temperatures where the FC and ZFC curve merge. The extracted blocking temperature was found to be highly correlated to NP size. Namely, the blocking temperature $T_B$ drastically increases with NP size. When below the blocking temperature, the particles progressively become magnetically frozen [10]. This prior magnetometry study suggests that there may be inter-particle coupling at low external field values that could cause interesting magnetic ordering within the ensembles of NPs. Additionally,

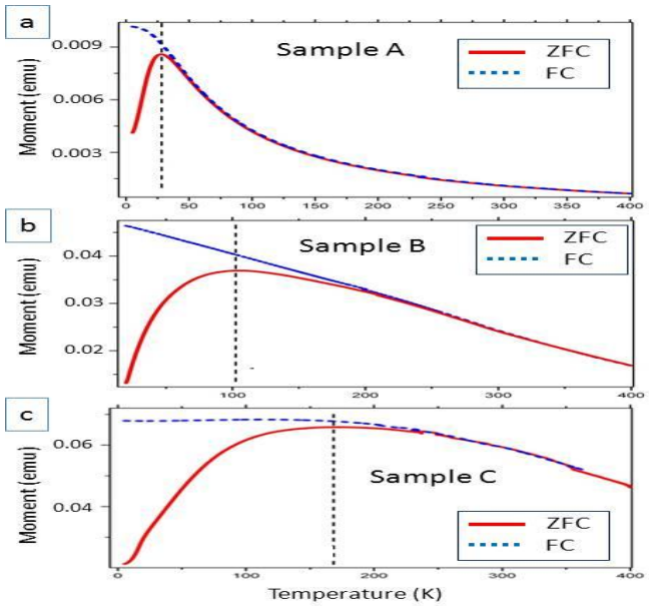


**Figure 1.3** ZFC/FC measurements of (a) sample A (5 nm), (b) sample B (8 nm), and (b) sample C (11 nm) measured at 100 Oe [10]. The temperature where the ZFC peaks is the blocking temperature and the further away from that point that the two curves merge again, the more inter-particle couplings that might be present in the sample.

VSM measurements provide only macroscopic averaged information. Information about nanoscale magnetic properties still need to be gained and is an active area of inquiry.

## 1.3 Problem Statement and Thesis

The prior work discussed above was primarily focused on characterizing the macroscopic properties of magnetite NP assemblies. We next aim to study the nanoscale magnetic ordering within the NP assemblies. To achieve this, we propose using three types of x-ray spectroscopy and scattering tools, discussed with further detail in their respective chapters:

1. X-ray resonant magnetic scattering (XRMS): the incoherent, azimuthally integrated scattering patterns can be used with our modeling techniques to characterize magnetic correlations.

2. X-ray resonant dichroic ptychography: ptychographic reconstruction of the associated real space images allows for direct inspection of ordering.

3. X-ray photon correlation spectroscopy (XPCS): the speckle pattern found in coherent diffraction patterns contains information about the magnetic ordering present in the illuminated sample.

We will discuss XRMS and its applications for modeling correlations in Chapter 2, how XRMS data can be used to perform dichroic ptychography in Chapter 3, and the use of XPCS in determining the dynamics of magnetic fluctuations in Chapter 4.

# Chapter 2

# Magnetic Correlation Modeling

## 2.1 Context

This work examines magnetite NP assemblies of two particle diameters, one of 5 nm and another of 11 nm. We prepared these samples in collaboration with Dr. Roger Harrison of the Brigham Young University Chemistry Department following an organic chemical synthesis [10–12]. The NP characteristics were determined in our lab via XRD, TEM, and VSM. The bulk of the data used in this work is comprised of x-ray resonant magnetic scattering (XMRS) diffraction images. These XRMS images were collected at opposite helicities of circular polarized light whose energy was tuned to the $L_3$ resonant edge of Fe for magneto-optical contrast. These data were collected at the Stanford Synchrotron Radiation Lightsource (SSRL) with an x-ray scattering setup detailed here [13]. When the x-ray energy is tuned to a resonant edge it provides necessary magneto-optical contrast to produce a magnetic scattering pattern. Additionally, the use of coherent x-rays generates a magnetic speckle pattern which constitutes a unique fingerprint of the magnetic ordering in real space at the time of illumination. By examining changes in the diffraction images through part of the magnetization loop it is possible to extract information about the local magnetic ordering as a

function of temperature and applied field for a given particle size. Attached here is the publication detailing our findings on the magnetic correlations found in our magnetite NP assemblies, and how the amount of magnetic ordering does not only depend on the magnetic field, but also on the temperature and size of nanoparticles. The data for this project was collected at the Standford Synchrotron Radiation Lightsource(SSRL). I handled the post-processing of the data, the model formulation and its application to the dataset, and writing of the relevant sections of the following publication.

## 2.2 Published Paper

I hereby confirm that the use of this article is compliant with all publishing agreements.

# Field-dependent nanospin ordering in monolayers of $Fe_3O_4$ nanoparticles throughout the superparamagnetic blocking transition

Johnathon Rackham,[1] Brittni Pratt,[1] Dalton Griner,[1] Dallin Smith,[1] Yanping Cai,[1] Roger G. Harrison,[2] Alex Reid,[3] Jeffrey Kortright,[4] Mark K. Transtrum,[1] and Karine Chesnel[1,*]

[1]*Department of Physics and Astronomy, Brigham Young University, Provo, Utah 84058, USA*
[2]*Department of Chemistry and Biochemistry, Brigham Young University, Provo, Utah 84058, USA*
[3]*SIMES, Stanford Linear Accelerator, Menlo Park, California 94025, USA*
[4]*Lawrence Berkeley National Laboratory, Berkeley, California 94720, USA*

(Received 22 November 2022; revised 14 July 2023; accepted 29 August 2023; published 15 September 2023)

We report on magnetic orderings of nanospins in self-assemblies of $Fe_3O_4$ nanoparticles (NPs), occurring at various stages of the magnetization process throughout the superparamagnetic (SPM)-blocking transition. Essentially driven by magnetic dipole couplings and by Zeeman interaction with a magnetic field applied out-of-plane, these magnetic orderings include a mix of long-range parallel and antiparallel alignments of nanospins, with the antiparallel correlation being the strongest near the coercive point below the blocking temperature. The magnetic ordering is probed via x-ray resonant magnetic scattering (XRMS), with the x-ray energy tuned to the Fe -$L_3$ edge and using circular polarized light. By exploiting dichroic effects, a magnetic scattering signal is isolated from the charge scattering signal. We measured the nanospin ordering for two different sizes of NPs, 5 and 11 nm, with blocking temperatures $T_B$ of 28 and 170 K, respectively. At 300 K, while the magnetometry data essentially show SPM and absence of hysteresis for both particle sizes, the XRMS data reveal the presence of nonzero (up to 9%) antiparallel ordering when the applied field is released to zero for the 11 nm NPs. These antiparallel correlations are drastically amplified when the NPs are cooled down below $T_B$ and reach up to 12% for the 5 nm NPs and 48% for the 11 nm NPs, near the coercive point. The data suggest that the particle size affects the prevalence of the antiparallel correlations over the parallel correlations by a factor ∼1.6 to 3.8 higher when the NP size increases from 5 to 11 nm.

DOI: 10.1103/PhysRevB.108.104415

## I. INTRODUCTION

The advance of nanotechnology heavily relies on our ability to manufacture high-quality nanostructured materials and control their behavior at the nanoscale. One type of material with high potentiality for magnetically based nanotechnologies is functional assemblies of magnetic nanoparticles (NPs) [1]. When their size is below ∼100 nm, magnetic NPs generally behave as individual nanomagnets, whose magnetization can be switched as a whole. A collection of such nanomagnets often presents interesting magnetic properties, including superparamagnetism (SPM) [2,3] and superferromagnetism [4,5]. These magnetic properties can be used in various applications, such as magnetic recording [6], magnetotransport [7], magnetoplasmonics [8], magnetocalorics [9], and for medical applications [10], such as contrast agents for magnetic resonance imaging [11], hyperthermia treatment, magnetic separation, and drug and gene delivery [12–17]. Due to its strong magnetization, its high chemical reactivity, and its nontoxicity [18], magnetite ($Fe_3O_4$) is well suited for these applications. To optimize the functionalities of magnetite NPs in the specific applications, it is important to understand and control the magnetic response of a collection of $Fe_3O_4$ NPs of different sizes to various stresses, such as the application of an external magnetic field, and the cooling and heating throughout the SPM blocking transition.

While the crystalline and magnetic properties of bulk $Fe_3O_4$ are well established [19], there is still knowledge to be gained about the magnetic behavior of collections of $Fe_3O_4$ NPs, depending on their size, shape, concentration, and type of magnetic interactions involved. At the atomic scale, the magnetization in $Fe_3O_4$ arises from the specific alignment of the spins carried by the $Fe^{2+}$ and $Fe^{3+}$ ions, which are distributed on a lattice of octahedral and tetrahedral sites throughout a spinel crystallographic structure [20]. Under exchange interactions, including Zener double exchange [21,22], the $Fe^{2+}$ and $Fe^{3+}$ spins align ferrimagnetically, thus yielding a net (nonzero) magnetic moment at the scale of the crystallites [23]. When in a NP form and if the NP size is below ∼125 nm [24], each NP is essentially monodomain (single magnetic domain extending throughout the NP) and therefore carries a massive magnetic moment, which we call *nanospin*.

When the NP size is smaller than ∼20 nm and if the distance between NPs is large enough so that interparticle interactions are negligible, a collection of $Fe_3O_4$ NPs typically exhibits SPM at room temperature, where each nanospin freely fluctuates independent of the neighboring nanospins but will eventually align under the application of an external

*kchesnel@byu.edu

 

magnetic field. However, there often exist nonnegligeable interparticle interactions, such as magnetic dipole interactions, causing the response of the material to deviate from the pure SPM behavior.

The interplay between the internal interparticle interactions and the Zeeman interaction induced by the external magnetic field can lead to various interparticle magnetic orderings, such as the parallel or antiparallel alignment of neighboring nanospins. For simplicity, we will, throughout the rest of this paper, use ferromagnetic (FM) to designate the parallel alignment and antiferromagnetic (AFM) to designate the antiparallel alignment of nanospins.

In this paper, we specifically focus on unveiling FM and AFM correlations that occur in the out-of-plane (OOP) direction between the nanospins in $Fe_3O_4$ NPs assemblies as a result of dipolar couplings and Zeeman interactions when applying an OOP magnetic field at various points in temperature throughout the SPM blocking transition. We probe the field dependence of the FM and AFM correlations when hysteresis occurs in the blocked phase below the blocking temperature.

The macroscopic magnetic behavior of $Fe_3O_4$ NPs and associated SPM-blocking transition have been widely studied via various techniques, such as magnetometry [25–28], Mössbauer spectrometry [29], electron paramagnetic resonance [27], and muon spin resonance [30]. To explain the observed data, particularly the relaxation dynamics of magnetic NPs in the SPM phase, sophisticated models have been developed, accounting for various magnetic anisotropies (magnetocrystalline, magnetostatic, strain, surface, and shape) but also for possible interparticle interactions [31]. Additionally, Mössbauer studies have allowed us to measure the effect of weak interparticle interactions on the SPM relaxation time [32]. However, this type of data is collected over a macroscopic number of NPs and does not provide spatial information about local nanoscale orderings. Limited work has been done to visualize the nanoscale magnetic correlations in assemblies of $Fe_3O_4$ NPs, using techniques such as magnetic force microscopy [33], x-ray magnetic spectroscopy [34], and neutron scattering [35], and the NP spatiotemporal behavior at the nanoscale still needs to be fully uncovered.

One particularly interesting question is how the individual nanospins tend to arrange when no longer aligned by an external magnetic field and Zeeman interaction is minimal. If the material is in the SPM phase, the net macroscopic magnetization $M$ of a NP assembly vanishes ($M = 0$) when the external magnetic field is released to zero ($H = 0$) due to spatial magnetic randomness combined with nanospin fluctuation over time. At the macroscopic scale $M = 0$, but at the microscopic scale, each NP still carries an intrinsic nanospin at any given time. An interesting question to explore is what kind of arrangements a collection of nanospins may generally adopt to yield $M = 0$. At any given time (setting magnetic fluctuations aside), both a random distribution of nanospins and an AFM arrangement of nanospins can yield $M = 0$. Additionally, one must account for possible fluctuations. While in the blocked phase, the magnetic order may remain static over a certain period of time, and nanospin fluctuations will eventually lead to $M = 0$ at higher temperature in the SPM phase. In our $Fe_3O_4$ NP assemblies, do interparticle magnetic correlations exist? If so, what is the nature of these correlations, and how do they depend on field, temperature, and particle size?

To answer these questions, one needs to probe NP materials at the nanoscale, and only a few techniques allow this to be done, including polarized electron microscopy, neutron scattering, and x-ray scattering. Small angle neutron scattering (SANS) [36] has traditionally been the method of choice to probe nanoscale magnetic correlations in magnetic materials. SANS studies have been carried on bulk $Fe_3O_4$ NPs [37]. However, there are a few limitations associated with neutron scattering techniques, particularly the need of massive samples to produce sufficient scattering signal, making data collection on thin monolayers of NPs challenging. Electron microscopy, on the other hand, allows the probing of very thin materials locally, offering subnanometric resolution. When polarized electron microscopy is available, it yields a magnetic contrast allowing one to identify the magnetic state of individual NPs [38]. However, polarized electron microscopy is challenging to implement and necessitates extremely thin materials that do not exceed a few nanometers, making the imaging of bigger NPs challenging.

To probe magnetic correlations in monolayers of $Fe_3O_4$ NPs, we utilize here an original synchrotron x-ray-based technique, x-ray resonant magnetic scattering (XRMS) [39], which allows one to surpass the mentioned limitations encountered with using neutrons or electrons. The use of synchrotron light enables the tunability of the x-ray energy to resonance edges of the magnetic elements contained in the material, here, the Fe-$L_3$ edge, providing element selectivity and magneto-optical contrast. At the Fe-$L_3$ edge energy $\sim$708 eV (soft x-ray range), the wavelength of the light is $\sim$1.75 nm, which is perfectly suited for accessing spatial correlations in the range of a few nanometers. Additionally, strong incident intensity and resonant scattering effects allow for rapid data collection from NP monolayers. Finally, the XRMS technique allows us to visualize magnetic correlations even when the net magnetization of the material is zero, which generally happens in SPM NPs when the magnetic field is released. XRMS is therefore a method of choice to study nanoscale magnetic correlations in NP monolayers.

Very few XRMS studies of magnetic NPs have been reported so far. In our previous study [40], we reported preliminary XRMS data collected at room temperature on monolayers of $Fe_3O_4$ NPs along with modeling [41]. Authors of previous studies on Co NP assemblies [42] have demonstrated the possibility to access interparticle magnetic correlation via the use of XRMS in linear polarization, by monitoring the variation of the XRMS signal with an external magnetic field. Here, we show a complementary approach by using XRMS in circular polarization and exploiting dichroic effects to extract information on the charge and magnetic correlations separately. We use this circularly polarized XRMS method to extract interparticle magnetic correlations on different sizes of $Fe_3O_4$ NPs, 5 and 11 nm, throughout the magnetization process at different temperatures above and below the SPM blocking transition.

## II. METHODS

Below, we provide details about the experimental steps and methods employed for this paper, including the NP

fabrication procedure, the transmission electron microscopy (TEM) imaging, the vibrating sample magnetometry (VSM) measurements, and the XRMS measurements using synchrotron radiation.

### A. NP fabrication

Our $Fe_3O_4$ NPs were prepared at Brigham Young University (BYU) via an organic solution method based on the thermal decomposition of an iron precursor in the presence of oleic acid. The use of oleic acid yields the formation of a ligand shell around each particle, which prevents particle clustering and leads to relatively uniform NP size. The particle size is tuned by adjusting various parameters in the preparation. Two particle sizes are considered in this paper: 5 nm (M5) and 11 nm (M11). The 5 nm particles were prepared via the thermal decomposition of $Fe(acac)_3$ in the presence of phenyl ether, hexadecane, oleylamine, and oleic acid at 275 °C for 30 min [43,44]. The 11 nm particles were prepared by heating an Fe(III) oleate in the presence of oleic acid and octadecene at 320 °C for 30 min [45]. After cooling to room temperature (25 °C), the NPs were precipitated in ethanol and separated by centrifugation at a speed of 5000 rpms for 15 min. After successive rounds of precipitation, a black powder was obtained, which was then used for the TEM, VSM, and XRMS measurements shown in this paper. Additionally, we have carried x-ray diffraction (XRD) measurements, already reported in Ref. [27], for which Rietveld refinements confirmed a nearly pure (>99%) magnetite $Fe_3O_4$ crystallographic phase. The XRD data also showed that the NPs are all monocrystalline.

### B. TEM imaging

To study their shape and size, the NPs were imaged via TEM. The TEM images were collected at BYU on a ThermoFisher Scientific Tecnai F20 UT instrument operating at 200 kV. For the TEM imaging, the NPs were deposited either on thin carbon membrane grids or silicon nitride ($Si_3N_4$) membranes. To prepare these TEM membranes, the prepared NPs, once in a powder form, were dissolved in either chloroform or toluene, and a drop of the solution was dropped onto the membranes, where the solvent would rapidly evaporate, leaving a self-assembly of NPs. The concentration of the solution was incrementally adjusted to achieve a monolayer of NPs, too concentrated solutions yielding multilayer stacking, while not enough concentrated solutions yielded sparse islands of NPs.

### C. Magnetization and field-cooling/zero-field-cooling data

The magnetization data were collected at BYU via VSM on a Quantum Design Physical Properties Measurement System that includes a 9 T superconducting magnet and a cryogenic sample holder using liquid helium allowing us to cool samples down to <10 K. For the VSM measurements, the NPs were inserted in a powder form into a capsule and compacted into a cylindrical pellet of ∼2 mm in diameter and 1 mm in thickness. The capsule was securely mounted on the VSM holder and tightened with quartz pieces to prevent internal motion while the holder was vibrating inside the detection coil. Magnetization loops were collected at various temperatures using a continuous sweeping of the superconducting magnet at ∼50 Oe/s. Zero-field-cooling (ZFC) and field-cooling (FC) data were collected by typically warming from 10 to 400 K at a speed of 1 K/s under a magnetic field of 100 Oe.

Powders of NPs were used for the magnetometry measurements because thin monolayers of NPs would not provide measurable VSM signal (and the membranes would break under the vibration). It is possible that the magnetic response of powders of NPs measured via VSM could slightly differ from the magnetic response of monolayers of the same NPs. However, as described in Sec. III, the TEM data show that the NPs in the assemblies tend to close pack, so it is reasonable to assume that the average interparticle distance is similar in the powders and films for a given NP size. Also, the TEM images show that the NPs are nearly spherical, so one can assume no significant magnetic shape anisotropy at the scale of the particles. When deposited in monolayers, it is possible that the overall sample shape anisotropy may affect the OOP magnetization loop. Unfortunately, the current VSM technology does not allow one to measure such data due to the insufficient amount of material in just a monolayer of NPs. However, our scattering results presented below indicate that the coercive point when applying an OOP field on two-dimensional (2D) layers coincides with the coercive point when measuring the magnetization on three-dimensional (3D) powders, so we can reasonably assume no significant differences between the 2D and 3D cases.

### D. XRMS

The XRMS data were collected on a coherent diffractive imaging instrument located at Beamline 13, at the Stanford Synchrotron Radiation Light Source (SSRL) synchrotron facility at Stanford Linear Accelerator Laboratory (SLAC). The x-ray light, produced by an elliptical polarization undulator was circularly polarized with a degree of polarization ∼99%. Deposited on thin $Si_3N_4$ membranes, the NP monolayers were probed in transmission geometry, with the x-ray beam at normal incidence, and 2D scattering patterns were measured downstream on a charge-coupled device (CCD) camera, as illustrated in our previous publication [40]. The 1″ square CCD detector included 2048×2048 pixels of 13×13 μm in size and was positioned at 10 cm downstream of the sample. The experiment was carried out in a vacuum scattering chamber to limit absorption of the soft x rays by air. The vacuum chamber included an electromagnet, allowing one to apply an *in situ* magnetic field from −3000 to +3000 Oe, in the direction of the incident x ray, i.e., OOP with respect to the membranes. In that geometry, the XRMS probe is essentially sensitive to the OOP component of the magnetization with respect to the plane of the layer. The instrument also included a cryogenic sample holder using liquid helium, allowing us to cool the samples down to 15 K. To optimize the magneto-optical contrast, the x-ray energy was finely tuned to a magnetic resonance at 706 eV, located within the $L_3$ edge of Fe. To find the exact energy of the magnetic resonance, prior x-ray magnetic circular dichroism (XMCD) data were collected under a magnetic field of ∼6000 Oe [34], showing a triple peak feature characteristic of $Fe_3O_4$. For the XRMS

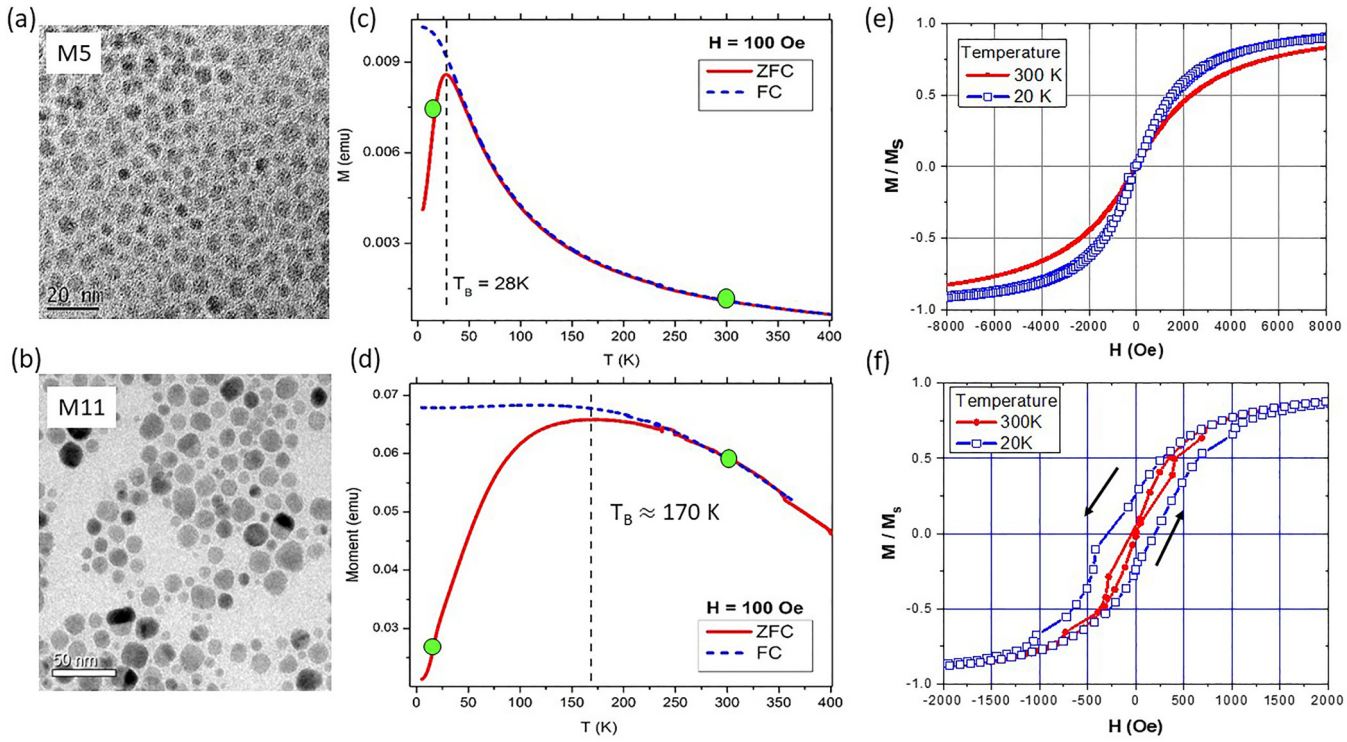


FIG. 1. Structural and magnetic properties of the 5 nm nanoparticles (NPs; M5) and 11 nm NPs (M11). (a) transmission electron microscopy (TEM) view of M5. (b) TEM view of M11. (c) and (d) Field-cooled (FC)/zero-field-cooled (ZFC) data measured via vibrating sample magnetometry (VSM) under a field $H$= 100 Oe on (c) M5 and (d) M11. (e) and (f) Magnetization loops measured via VSM at 300 and 20 K on (e) M5 and (f) M11, respectively. The temperature points for magnetization data are located by green dots on the FC/ZFC curves. The TEM images were collected on thin monolayers of NPs, whereas the VSM data were collected on powders made of same NPs.

measurement, the x-ray energy was set to the first peak at 706 eV. To separate the magnetic scattering signal from the charge scattering signal, the XRMS data were collected at opposite helicities of circular polarization. The exposure and collection time combined was ∼20 s per CCD image. To increase the signal to noise, typically 10 of these images were successively collected, for a total measurement time of ∼200 s at a given temperature, field, and polarization and averaged to extract the XRMS signal presented in this paper.

### E. Data fitting

The data were fit using the Python library LMFIT, a useful extension of the SCIPY optimization methods, for nonlinear least-squares minimization to fit the charge intensity and magnetic ratio curves [46]. We used the implementation of the Levenberg-Marquardt algorithm (LMA) found in LMFIT for the residual optimization. Further discussion of the model used for the fitting process can be found in Sec. V.

## III. MATERIAL PROPERTIES

Here, we describe the basic structural and magnetic properties of the studied NPs. Information about the particle shape, size, and tendency to self-assemble is obtained from TEM images. Information about the SPM blocking transition and associated blocking temperature is extracted from ZFC/FC curves. Finally, the occurrence of hysteresis is discussed based on magnetization data.

### A. Structural properties

The TEM image of M5 in Fig. 1(a) indicates that the 5 nm NPs are typically spherical and relatively uniform in size. A statistical analysis of a collection of NPs on the image yields an average particle size of $5.3 \pm 0.7$ nm. The TEM image shows that the NPs tend to self-assemble in a closely packed hexagonal lattice, forming a uniform monolayer.

The TEM image of M11 in Fig. 1(b) shows that the 11 nm NPs are also spherical but less uniform in size. The statistical analysis yields an average particle size of $11.3 \pm 2.5$ nm. These NPs also tend to self-assemble in a hexagonal manner, but due to the wider size distribution, the extent of the lattice is spatially limited, leading to sparse islands with different orientations. The sharp change in contrast visible within some NPs suggests occasional crystal twinning. The magnetization and XRMS data, however, indicate that the NPs essentially remain magnetically monodomain.

### B. SPM blocking transition

The ZFC/FC data collected at 100 Oe on M5 in Fig. 1(c) show a very sharp transition between the SPM and blocked states, with a blocking temperature $T_B = 28$ K. The sharpness of the transition reflects the narrow size distribution.

The ZFC/FC data collected at 100 Oe on M11 in Fig. 1(d) show a broader transition with an average blocking temperature $T_B \sim 170$ K. The drastic increase in $T_B$ is due to the increase in NP size from 5 to 11 nm. The peak broadening reflects the wider size distribution.

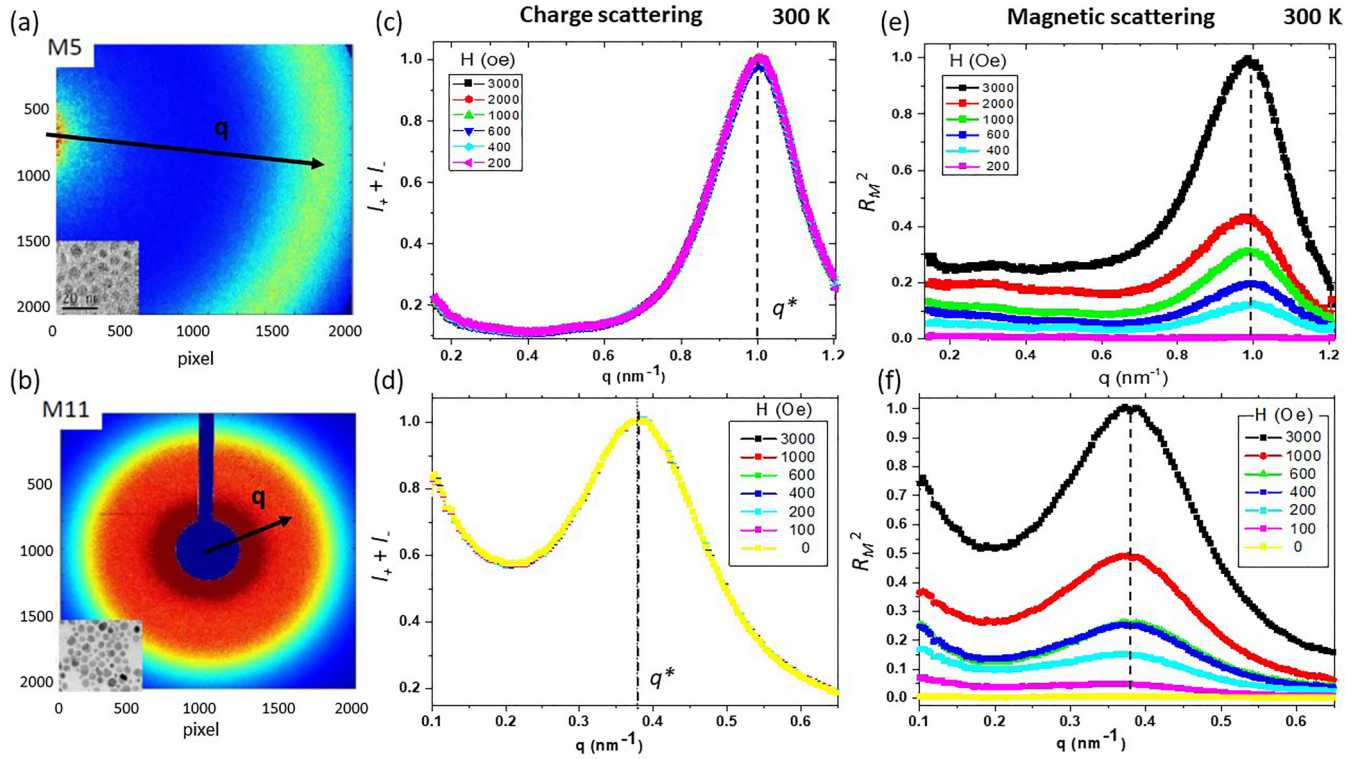


FIG. 2. Two-dimensional (2D) x-ray resonant magnetic scattering (XRMS) patterns measured for (a) M5 and (b) M11 at the Fe-$L_3$ edge. (c)–(f) Extracted charge and magnetic scattering profiles after azimuthal integration of the 2D patterns and combination of intensities $I_+(q)$ and $I_-(q)$ measured in opposite helicities of the circular light, shown at various applied magnetic field values $H$, from 3000 Oe down to zero. The charge scattering signal is $I_+ + I_-$, with peak at $q^*$ normalized to 1, in (c) for M5 and in (d) for M11. The magnetic scattering signal is $R_M^2 = (I_+ - I_-)^2/(I_+ + I_-)$ with peak at $q^*$ normalized to 1 for the highest field value $H$= 3000 Oe, in (e) for M5 and in (f) for M11.

### C. Magnetization data

Magnetization loops were measured at 300 K (above $T_B$) and at 20 K (below $T_B$). These points in temperature are indicated by green dots on the ZFC/FC curves. The magnetization loops for M5 in Fig. 1(e) show a smooth S shape, which can be modeled by the Langevin function, characteristic of SPM. The absence of hysteresis confirms a pure SPM phase for the 5 nm particles. For M11, the magnetization loops shown in Fig. 1(f) reveal very little hysteresis at 300 K but some significant hysteresis, up to $H_c = 300$ Oe at 20 K, well below $T_B$.

Magnetic hysteresis typically occurs when the NPs are in their blocked state and exhibit internal magnetic anisotropy. There are multiple possible sources of anisotropies in crystalline magnetic NPs, including magnetocrystalline anisotropy, surface anisotropy, and shape anisotropy [32]. In the case of our $Fe_3O_4$ NPs, the TEM micrographs showed that the NPs are mostly spherical and therefore do not exhibit significant magnetic shape anisotropy. Other types of anisotropy such as magnetocrystalline and surface anisotropies are likely present, although not strong enough to induce significant hysteresis. On the other hand, our XRMS data show the presence of enhanced interparticle magnetic correlations below $T_B$ near the coercive point. While the XRMS data do not allow us to determine the cause of hysteresis, these observations suggest that the magnetic hysteresis may not result solely from magnetic anisotropies but also from combined interparticle magnetic couplings.

## IV. X-RAY MAGNETIC SCATTERING RESULTS

To investigate the nanoscale magnetic orderings between the NPs, we collected XRMS data on monolayers of the various $Fe_3O_4$ NPs. In our previous work [40], we showed how the x-ray energy is first tuned to the Fe-$L_3$ edge using XMCD and demonstrated how to exploit the polarization of the light to extract a magnetic signal from the scattering patterns. For this purpose, we introduced a magnetic ratio $R_M$ aimed to isolate the magnetic signal from the charge signal in the scattering patterns. Here, we apply this approach to probe magnetic orderings that may occur with the OOP component of the nanospins and compare them with the charge ordering within the NP monolayer throughout the SPM blocking transition. First, we show 2D scattering patterns and their associated one-dimensional (1D) scattering profiles. We then review the steps for separating the magnetic signal from the charge signal in these 1D profiles. Finally, we look at the dependence on magnetic field and on temperature for the 5 and 11 nm NPs.

### A. Charge and magnetic scattering signal separation

The XRMS patterns collected on M5 [Fig. 2(a)] and M11 [Fig. 2(b)] inform on the lattice formed in the respective NP assemblies. Both patterns have the shape of a ring, here in the momentum space. The ring radius is inversely proportional to the average interparticle distance in the NP assembly. The radius is larger for M5 than for M11, consistent with a smaller

interparticle distance for the 5 nm NPs. Also, the ring is relatively narrower for M5, reflecting a more highly ordered NP lattice than for the 11 nm NPs.

To extract quantitative information on the charge structure and the magnetic structure in the NP assemblies, we first integrated the 2D scattering patterns azimuthally to generate 1D datasets of the scattering intensity $I(q)$ as a function of the momentum $q$. Next, we separated the charge scattering from magnetic scattering signal by exploiting the light polarization as follows. As derived in Ref. [47], the scattering intensity may be written in terms of scattering amplitudes:

$$I_{\pm} = |A_c \pm A_m|^2 = |A_c|^2 \pm (A_c A_m^* + A_m A_c^*) + |A_m|^2,$$

where $I_+$ and $I_-$ represent the scattering intensity collected with positive and negative circular polarization, respectively; $A_c$ and $A_m$ represent the amplitudes of the charge and magnetic scattering, respectively. By construction, $A_c$ and $A_m$ are complex quantities, and the * symbol denotes the complex conjugate. To separate $A_c$ and $A_m$, at first order, the following approach is adopted. On one hand, we consider the average of intensities between opposite helicities of the circular polarization (which also corresponds to the intensity $I_0$ one would measure in linear polarization):

$$I_0 = (I_+ + I_-)/2 = |A_c|^2 + |A_m|^2.$$

In our specific dataset, however, $|A_m|^2$ turns out to be negligible compared with $|A_c|^2$. Consequently:

$$I_0 = (I_+ + I_-)/2 \approx |A_c|^2.$$

This approach differs from another approach adopted in other studies [45], where the sum $I_+ + I_-$ is compared at different field values $H$, typically at saturation and remanence ($H = 0$), and the difference gives access to the magnetic part $|A_m|^2$. In our case, the sum $(I_+ + I_-)$ $(q)$ shows visibly no dependence with $H$, as demonstrated in Figs. 2(c) and 2(d) for M5 and M11, respectively, confirming that $|A_m|^2 \ll |A_c|^2$ here. Additionally, the fact that $|A_c|^2$ is essentially not changing when $H$ is varied indicates that the NPs, sitting solidly on the membrane, are not physically moving when applying a magnetic field up to 3000 Oe.

On the other hand, we consider the difference of the scattering intensities measured at opposite helicities:

$$I_+ - I_- = 2(A_c A_m^* + A_m A_c^*) = 2\mathrm{Re}(A_m A_c^*).$$

This difference, a real number, may be either positive or negative in sign and will typically switch sign when the internal magnetization of the material is reversed via the reversal of the applied magnetic field, as demonstrated by our previous studies [40]. As it is conventionally done in XMCD, a dimensionless dichroic ratio may be derived from the difference:

$$R_D = \frac{I_+ - I_-}{I_+ + I_-} = \frac{2\mathrm{Re}(A_m A_c^*)}{2(|A_c|^2 + |A_m|^2)} \approx \frac{\mathrm{Re}(A_m A_c^*)}{|A_c|^2}.$$

However, $R_D$ depends on both $A_c$ and $A_m$ amplitudes. Our approach is to instead consider the following magnetic ratio $R_M$:

$$R_M = \frac{I_+ - I_-}{\sqrt{I_+ + I_-}} = \frac{\sqrt{2}\,\mathrm{Re}(A_m A_c^*)}{\sqrt{|A_c|^2 + |A_m|^2}} \approx \frac{\sqrt{2}\,\mathrm{Re}(A_m A_c^*)}{|A_c|}.$$

Now our data suggest that there is no significant dephasing between $A_c$ and $A_m$, so here, $\mathrm{Re}(A_m A_c^*) \approx |A_c||A_m|$, and consequently, $R_M$ does not much depend on the charge scattering amplitude $|A_c|$ but essentially relies on the magnetic scattering amplitude:

$$R_M \propto |A_m|.$$

That way, the magnetic signal can be separated from the charge signal to a first approximation. Incidentally, $R_M$ not only depends on the magnitude of $A_m$ but also, via the phase factor, switches sign when the magnetization of the material is reversed. To compare the charge scattering and magnetic scattering signals having same dimension, we chose to consider the square of $R_M$:

$$R_M^2 \propto |A_m|^2,$$

which, like $I_0$, has the dimension of an intensity.

In summary, we focus here on two independent quantities that provide us with information on the charge structure and the magnetic structure in the material:

$$I_0 \approx |A_c|^2(q), \quad R_M^2 \approx |A_m|^2(q).$$

As an illustration, $R_M^2$ is represented next to its associated $I_0$ signal in Figs. 2(e) and 2(f), for M5 and M11, respectively. These data are measured at 300 K with $H$ varying from 3000 Oe to zero. For both M5 and M11, $R_M^2$ drastically varies with $H$. Not only the magnitude of $R_M^2$ gradually decreases all the way down to near zero when $H$ is decreased to zero, confirming the magnetic nature of $R_M^2$, but its shape (dependence on $q$) changes too, indicating changes in magnetic density within the material.

The dependence of $R_M^2$ on the momentum $q$ contains spatial information on the nanoscale magnetic ordering. In this paper, we study how the shape of $R_M^2(q)$ varies with $H$ throughout the magnetization process and with temperature $T$ when cooling down below the SPM blocking transition, for each of the two particle sizes. For comparison purposes, we show, in the subsequent figures, a normalized version of $|R_M|(q)$, where the magnitude of the main peak (located at $q^*$) is normalized to 1. Comparing the shape of $|R_M|(q)$ allows us to identify the emergence of various magnetic orders, such as FM and AFM orders. We later quantify the amount of respective FM and AFM orders, but rather than using the absolute magnitude of $|R_M|(q)$ which we found unreliable (due to various experimental instabilities), we used the relative magnitudes of the FM and AFM signals combined with magnetization data.

### B. Results for 5 nm particles

The charge scattering signal plotted in Fig. 2(c) shows a peak at $q^* \approx 1.0\,\mathrm{nm}^{-1}$, suggesting an average interparticle distance $p_0 = 2\pi/q^* \approx 6.3$ nm for M5. Given the particle average size of ~5.3 nm, this leaves an average gap between particles of ~1 nm, which is about the size of the oleic acid ligand shell. This confirms that the 5 nm NPs are mostly close packed, forming a hexagonal lattice, as suggested by the TEM images on smaller fields of view.

The magnetic scattering signal at 300 K plotted in Fig. 2(e) shows a peak located at the same location $q* \approx 1\,\mathrm{nm}^{-1}$. This indicates the presence of magnetic correlations in the NP

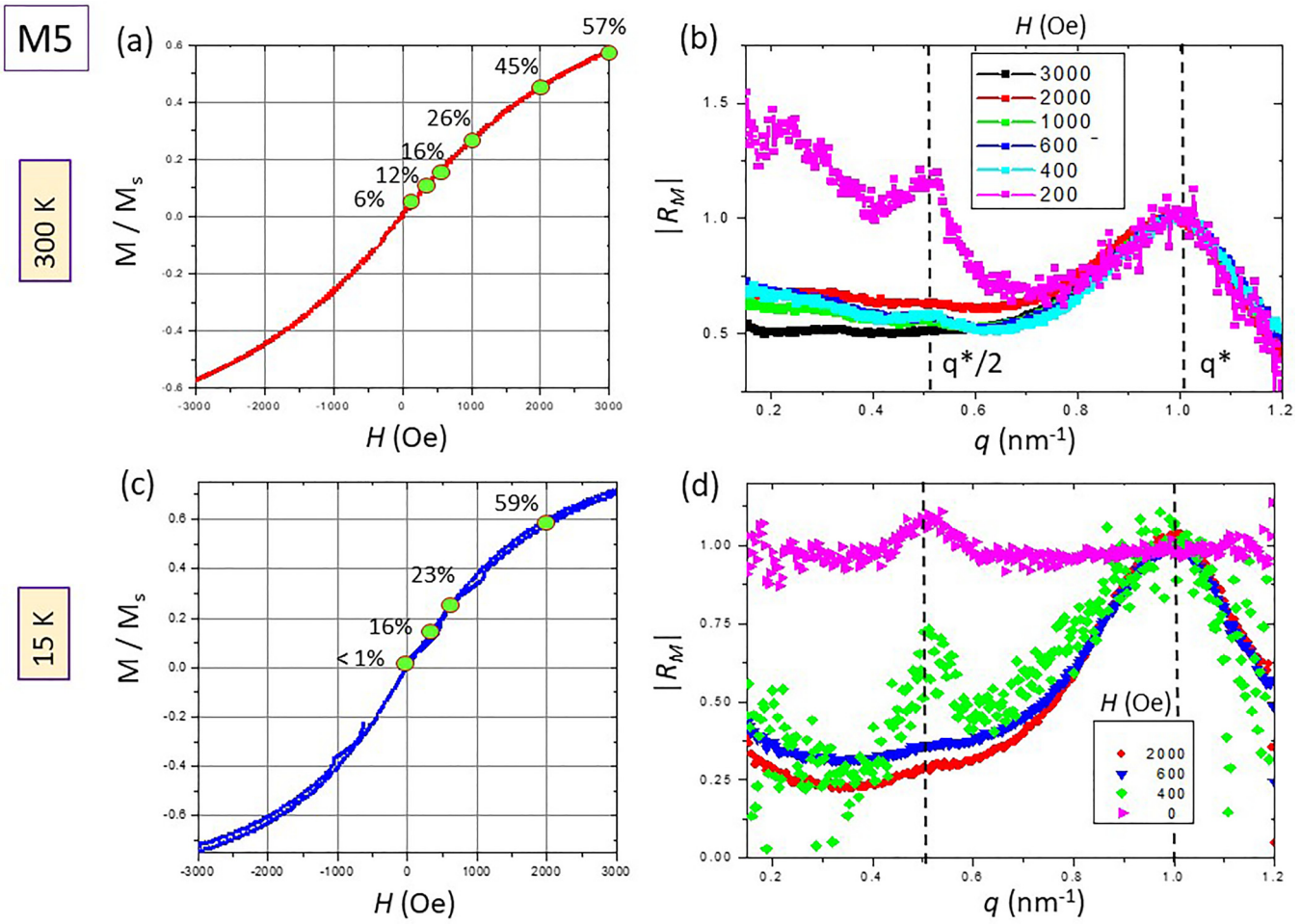


FIG. 3. X-ray resonant magnetic scattering (XRMS) results for M5 at 300 K and 15 K. (a) Normalized magnetization curve $M(H)$ measured at 300 K in the ±3000 Oe range. (b) $|R_M|(q)$ data measured at 300 K at the various $H$ values indicated on the $M(H)$ curve (a). (c) Normalized magnetization curve $M(H)$ measured at 15 K in the ±3000 Oe range. (d) $|R_M|(q)$ data measured at 15 K, at the various $H$ values indicated on the $M(H)$ curve (c). For (b) and (d), the $|R_M|(q)$ data are normalized to set the value of the peak at $q^*$ to 1.

assembly, namely, a FM ordering of the nanospins, where the magnetic period matches the structural one: $p_{\mathrm{FM}} = p_0$. In this configuration, most of the nanospins point in the direction set by the external field. The FM signal is the strongest at the highest field value $H$= 3000 Oe and progressively decreases when $H$ is decreased, as the internal net magnetization $M$ also decreases.

Figure 3 shows the evolution of normalized $|R_M|(q)$ with magnetic field for M5 at 300 K above $T_B$ and at 15 K below $T_B$. On the left side, a zoomed-in view of the magnetization curve $M(H)$ in the range of [−3000 Oe, +3000 Oe] is plotted, showing the various points in field $H$ where XRMS data were collected. Next to each point, the associated degree of magnetization $M$, normalized to magnetization at saturation $M_s$, is indicated (in %). The $|R_M|(q)$ data at 300 K in Fig. 3(b) show a single FM peak at $q^*$ for most field values $H$ from 3000 to 400 Oe. Only when $H \leqslant 200$ Oe, an additional peak around $q^*/2$ emerges, suggesting the presence of some linear AFM ordering of nanospins, for which the periodicity is $p_{\mathrm{AF}} = 2p_0$. This AFM peak is, however, much weaker than the FM peak, seemingly less than half of it. Given that, at $H$= 200 Oe, the net magnetization $M$ is only 6% of the magnetization at saturation $M_s$, the amount of FM correlations covers only ∼6%, and therefore, the amount of AFM correlations is relatively small, seemingly <3% (the data fitting described in the next sections consistently shows that this quantity is closer to 2.3%).

The behavior at $T$= 15 K, below $T_B$, is like that at 300 K, except that the AFM peak emerges a bit earlier, at $H$= 400 Oe, when $H$ is decreased and becomes relatively stronger than the FM peak when $H$ approaches zero. No hysteresis was observed in the magnetization curve $M(H)$, so a symmetrical behavior is expected in respect to switching the sign of $H$.

### C. Results for 11 nm particles

The charge scattering signal for M11, plotted in Fig. 2(d), shows a peak at $q^* \approx 0.38\,\mathrm{nm}^{-1}$, which corresponds to an average interparticle distance of ∼16.5 nm. Given the particle average size of 11.3 nm, this leaves an average gap between particles of ∼5.2 nm. This loose gap accounts for the wide distribution of NP sizes, which prevents the NPs from closely packing in large areas but rather allows the NPs to form sparse islands, as seen on the TEM image Fig. 1(b).

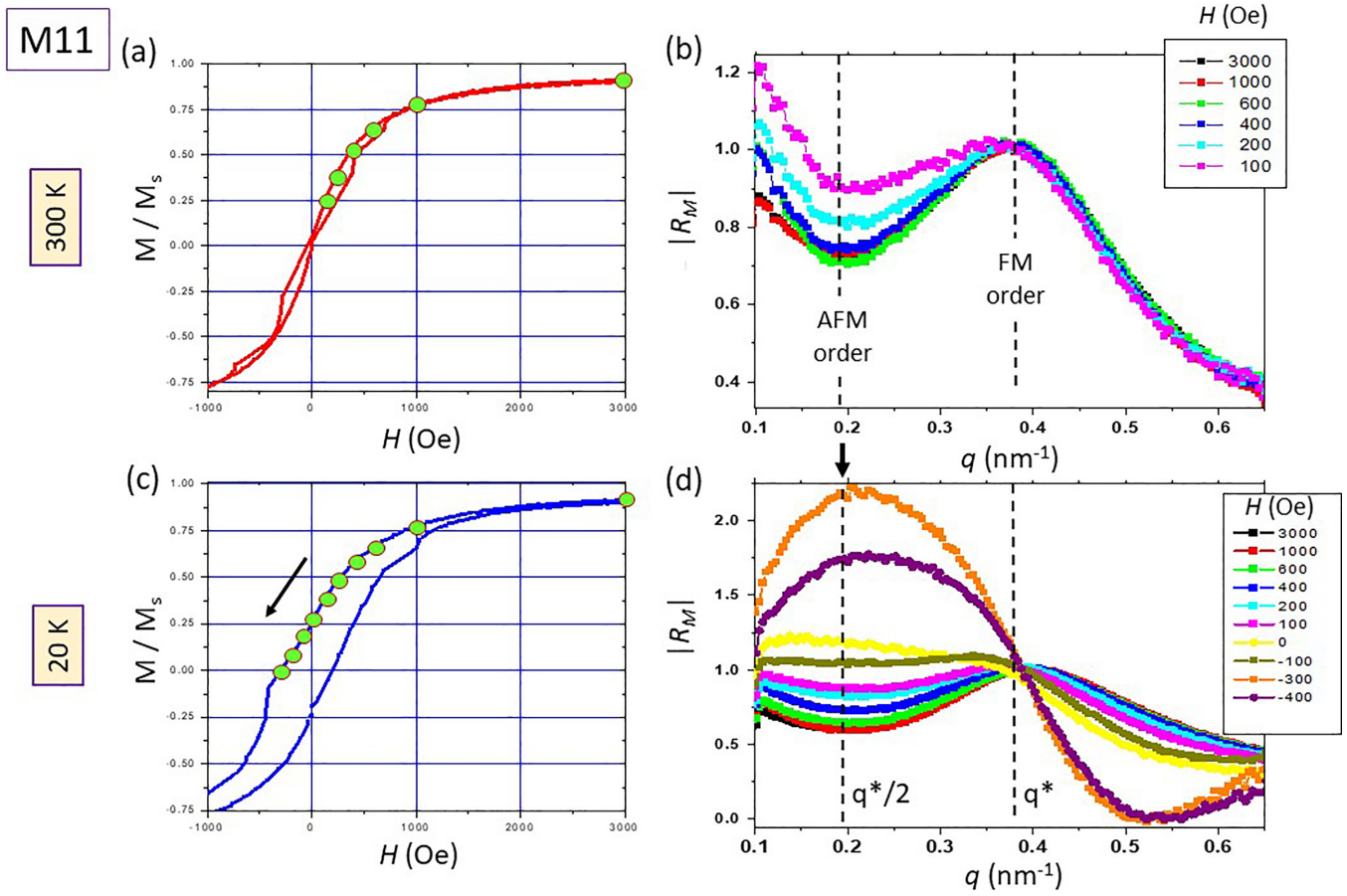


FIG. 4. X-ray resonant magnetic scattering (XRMS) results for M11 at 300 and 20 K. (a) Normalized magnetization curve $M(H)$ measured at 300 K, focusing on the positive branch. (b) $|R_M|(q)$ data measured at 300 K at the various $H$ values indicated on the $M(H)$ curve (a). (c) Normalized magnetization curve $M(H)$ measured at 20 K showing hysteresis, with coercive field $|H_c| \approx 300$ Oe. (d) $|R_M|(q)$ data measured at 15 K, at the various $H$ values indicated on the $M(H)$ curve (c) from +3000 Oe down to −400 Oe, past the coercive point. For (b) and (d), the $|R_M|(q)$ data are normalized to set the value of the peak at $q^*$ to 1.

The normalized magnetic ratio signal $|R_M|(q)$ for M11 is shown in Fig. 4, both at 300 K above $T_B$ [Figs. 4(a) and 4(b)] and at 20 K well below $T_B$ [Figs. 4(c) and 4(d)]. In contrast with M5, the data for M11 generally show a more pronounced dependence of the shape of $R_M^2(q)$ on the magnetic field $H$. The $|R_M|(q)$ data in Fig. 4(b) collected at 300 K and $H$= 3000 Oe show essentially one single peak, located at the same $q^*$ as the peak in the charge scattering signal in Fig. 2(d), corresponding to FM ordering. When the field $H$ is lowered, the FM peak remains present, but the magnitude of the signal at around $q^*/2$ progressively increases, suggesting the gradual emergence of some AFM correlations in the NP assembly. The AFM signal remains, however, limited, dominated by the FM signal.

At 20 K, on the other hand, the progression is significantly more drastic. While at $H$= 3000 Oe, the system shows mostly FM ordering with a main peak at $q^*$, the shape of $|R_M|(q)$, however, drastically changes when the field $H$ is lowered, and an AFM signal extended on a wide $q$ range near $q^*/2$ arises and eventually surpasses the FM signal. At 20 K, M11 shows hysteresis, so at $H$= 0, there is still a strong remanence ($M/M_s \approx 25\%$). When further decreasing $H$ down to negative values, the AFM signal then strikingly increases, far dominating the FM signal, and reaches a maximum value at the coercive point $H = -H_c = -300$ Oe.

The data on M5 and M11 undeniably show the emergence of some AFM ordering of OOP nanospins, when the NP assembly is cooled down below $T_B$ and when $H \sim 0$. It also shows that the amount of AFM correlations with respect to the amount of FM correlations depends on particle size. The data here suggest that the smaller 5 nm NPs tend to orient mostly randomly when the field is released to zero, whereas the bigger 11 nm particles show significant AFM correlations that are the strongest when the field is brought to the coercive point.

To solidify these qualitative observations, we fitted the data using an empirical model, which provides quantitative information about the various magnetic orders in the NP assemblies, including their relative amounts and their associated periodicities and correlation lengths.

## V. DATA FITTING

Here, we describe the empirical model we utilized to fit both the charge and the magnetic components of the x-ray scattering data. The primary goal of this fitting work is to

TABLE I. List of the parameters used in the global fit of the charge and magnetic scattering data.

| Parameter | Description | Boundaries constraints | Symbol for associated physical quantity |
|---|---|---|---|
| $b_1$ | Charge central amplitude | $b_1 \geqslant 0$ | $A_0$ |
| $b_2$ | Charge central width | $b_2 > 0$ | $\omega_0$ |
| $b_3$ | Charge peak amplitude | $b_3 \geqslant 0$ | $A_c$ |
| $b_4$ | Charge peak position | $b_4 > 0$ | $q^*$ |
| $b_5$ | Charge peak width | $b_5 > 0$ | $\omega_c$ |
| $b_6$ | Charge baseline | $b_6 \geqslant 0$ | $B_c$ |
| $c_1$ | Magnetic central amplitude | $c_1 \geqslant 0$ | $A_1$ |
| $c_2$ | Magnetic central width | $0 < c_2 \leqslant 1$ | $\sigma_1$ |
| $c_3$ | FM amplitude | $c_3 \geqslant 0$ | $A_{\mathrm{FM}}$ |
| $c_4$ | FM peak position | $q^* \pm \varepsilon$ | $q_{\mathrm{FM}}$ |
| $c_5$ | FM width | $0 < c_5 \leqslant \sigma_{\max}$ | $\sigma_{\mathrm{FM}}$ |
| $c_6$ | AFM amplitude | $c_6 \geqslant 0$ | $A_{\mathrm{AF}}$ |
| $c_7$ | AFM peak position | $q^*/2 \pm \varepsilon$ | $q_{\mathrm{AF}}$ |
| $c_8$ | AFM width | $0 < c_8 \leqslant \sigma_{\max}$ | $\sigma_{\mathrm{AF}}$ |
| $c_9$ | Magnetic baseline | $c_9 \geqslant 0$ | $B_m$ |

obtain quantitative information on the various magnetic ordering components present in the material and their dependence with field and temperature for each particle size. Below, we review the model used for the fit, its mathematical formulation, and its associated parameters. We then describe how the fit was conducted and optimized as a global fit on the charge and magnetic components at different field values.

### A. Model

We adopt here an empirical model consisting of fitting the scattering data directly in the $q$ space. Best results were obtained with Lorentzian functions for fitting the charge scattering signal $I_0$ and with Gaussian functions for fitting the magnetic scattering signal $|R_M|$.

First, we fit the charge scattering signal $I_0 = (I_+ + I_-)/2$, which generally exhibits one main peak, sitting over a diffuse scattering background, using a combination of Lorentzian functions:

$$I_0(\mathbf{b};q) = b_1 \frac{b_2}{q^2 + b_2^2} + b_3 \frac{b_5}{(q-b_4)^2 + b_5^2} + b_6,$$

where $\mathbf{b} = (b_1, b_2, \ldots, b_6)$ represents the fitted parameters. The parameters $b_1$ and $b_2$, respectively, represent the magnitude and width of the diffuse scattering signal centered at $q = 0$. The parameters $b_3$, $b_4$, and $b_5$, respectively, represent the magnitude, position, and width of the charge scattering peak centered at $q = q^*$, and the parameter $b_6$ represents a baseline. Once the peak position and width are fitted to optimal values ($b_4 = q^*$, $b_5 = \omega_c$), we estimate the charge correlation period $p_0 = \frac{2\pi}{q^*}$, interpreted as the average interparticle distance, and associated correlation length $\lambda_c = \frac{2\pi}{\omega_c}$.

Next, we fit the magnetic signal $|R_M|(q)$, which usually includes a mix of interparticle magnetic orders. The model function to fit the $|R_M|$ data consist of three pieces: a Gaussian function centered at $q = 0$ with an associated baseline constant to account for the diffuse magnetic scattering signal and for random orientation of nanospins, a Gaussian function accounting for the FM ordering, and a Gaussian function accounting for the AFM ordering. The AFM order corresponds to an up/down alternation of neighboring nanospins. If occurring along one given direction (1D) in the material, this alternation theoretically yields a magnetic periodicity that is twice that of the FM order: $p_{\mathrm{AF}} = 2p_{\mathrm{FM}}$. The associated AFM scattering signal should then be located near $q \approx q^*/2$. In practice, the fitted location $q^*$ for the charge peak could be used to set the target locations of the FM and AFM peaks, around $q^*$ and $q^*/2$, respectively. However, the XRMS data show that the AFM signal is often extended on a wide range of $q$ values near but not necessarily centered on $\frac{q^*}{2}$. We therefore set the position of both the FM and AFM components free to be fitted. The modeled quantity $|R_M|$ is then written as follows:

$$\begin{aligned}|R_M|(\mathbf{c};q) = {} & \frac{c_1}{c_2\sqrt{2\pi}} \exp\left(-\frac{q^2}{2c_2^2}\right) \\ & + \frac{c_3}{c_5\sqrt{2\pi}} \exp\left[-\frac{(q-c_4)^2}{2c_5^2}\right] \\ & + \frac{c_6}{c_8\sqrt{2\pi}} \exp\left[-\frac{(q-c_7)^2}{2c_8^2}\right] + c_9,\end{aligned}$$

where $\mathbf{c} = (c_1, c_2, \ldots, c_9)$ represents a set of fitted coefficients in our model. The coefficient $c_1$ is the relative amplitude of the central diffuse magnetic scattering signal, $c_2$ its width, $c_3$ the relative amplitude of the FM scattering signal, $c_4$ its position (set free to deviate from $q^*$ within $\pm\,\varepsilon$), $c_5$ its width, $c_6$ the relative amplitude of the AFM scattering signal, $c_7$ its position (set free to deviate from $\frac{q^*}{2}$within $\pm\,\varepsilon$), $c_8$ its width, and $c_9$ the relative height of an empirical baseline. All the fitting parameters along with their descriptions, their associated boundaries, and the physical symbols associated with them are summarized in Table I.

The fitted parameters are used to calculate the following quantities: the FM correlation period $p_{\mathrm{FM}} = 2\pi/q_{\mathrm{FM}}$ and associated correlation length $\lambda_{\mathrm{FM}} = 2\pi/\sigma_{\mathrm{FM}}$; the AM correlation period $p_{\mathrm{AF}} = 2\pi/q_{\mathrm{AF}}$ and associated correlation length $\lambda_{\mathrm{AF}} = 2\pi/\sigma_{\mathrm{AF}}$. The relative amplitudes $A_{\mathrm{FM}}$ and $A_{\mathrm{AF}}$ of the FM and AFM signals are used to quantify the respective

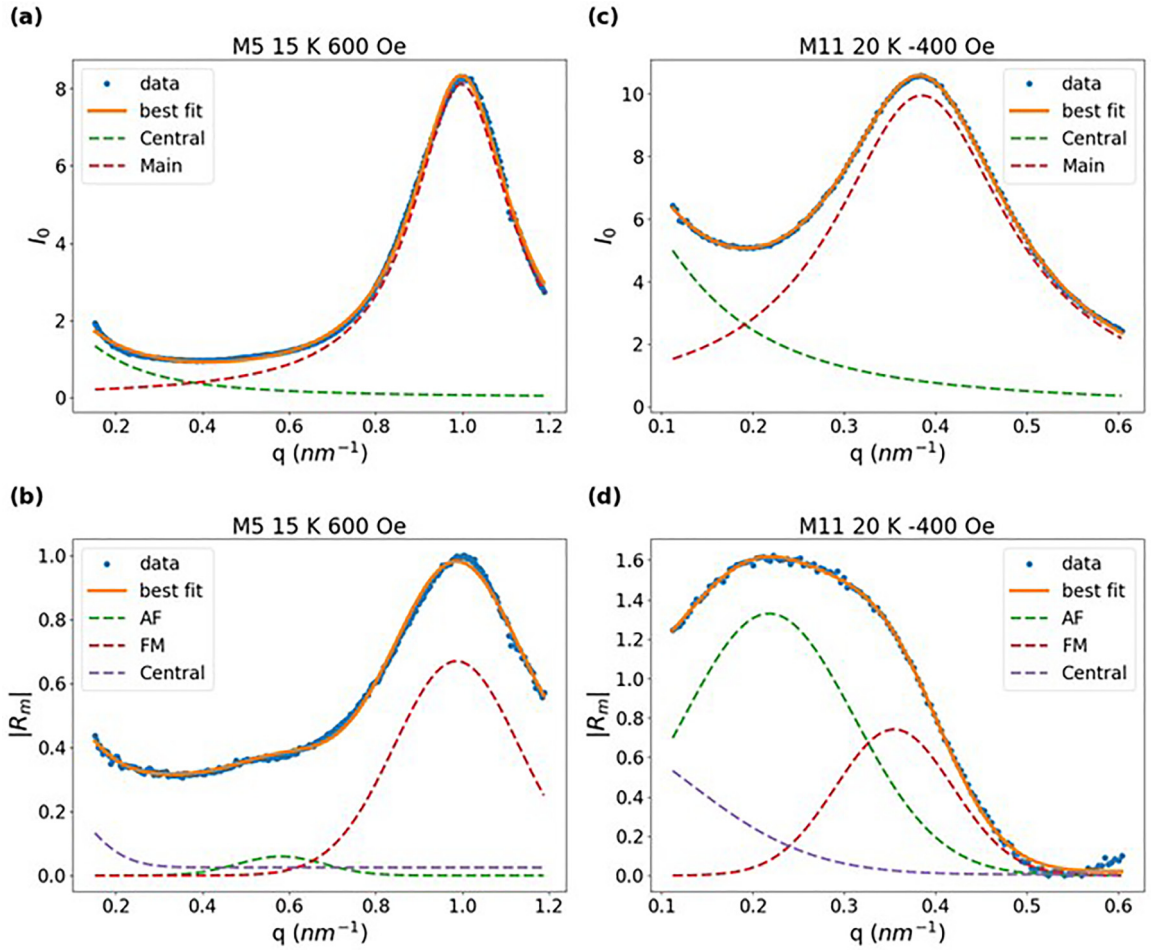


FIG. 5. Illustration of the fits carried on the charge scattering intensity $I_0$ and magnetic ratio $R_m$ signals. $I_0$ was fitted using Lorentzian functions and $R_m$ using Gaussian functions. In each case, individual Lorentzian/Gaussian components are shown in dashed lines. (a) Fit of $I_0$ and (b) fit of $R_m$ for M5 at 15 K and $H = 600$ Oe. (c) Fit of $I_0$ and (b) fit of $R_m$ for M11 at 20 K and $H = -400$ Oe.

concentrations (in %) of the FM and AFM correlations in the NP assembly. In this estimation, we set the FM concentration to be equal to the normalized net magnetization $M/M_s$ since the net magnetization essentially results from FM aligned nanospins.

### B. Synchronous fit of charge and magnetic signals

This global fit was done using the Python library LMFIT and its extension of the LMA to find the best fit parameters within a restricted domain. The allowed domain for $c_5$ is $q^* \pm \varepsilon$. For M5, $q^* = 1.00\,\mathrm{nm}^{-1}$ and $\varepsilon = 0.08\,\mathrm{nm}^{-1}$ (8% of $q^*$), whereas for M11, $q^* = 0.38\,\mathrm{nm}^{-1}$ and $\varepsilon = 0.06\,\mathrm{nm}^{-1}$ ($\sim$16% of $q^*$). Another important constraint is the range for the Gaussian widths $\sigma$. Its upper limit $\sigma_{\max}$ corresponds to the lower limit of possible correlation lengths, which we set to the average interparticle distance, namely, $\sigma_{\max} = 2p/p_0$. These constraints, summarized in Table I, restrict the domain of the parameters sufficiently to maintain our mechanistic interpretation of the model.

The dataset is comprised of points for each sample at different applied magnetic field values and temperatures. For each field value and temperature, we first fit the charge signal to determine the value of $q^*$, which sets the boundary constraints for the fitting of the $R_m$ signal. The choice of initial parameter values has a large effect on the results of the LMA. To ensure that we escape local minima, we run the LMA on each data point 300 times with each time the new initial parameter guess being a small random deviation from the previous best fit result.

We estimate the standard error in the parameters using the method employed in the LMFIT library, namely, the square roots of the diagonal elements of the covariance matrix calculated from the model residual Jacobian evaluated at the best fit parameter values. For the error associated with figures of interest derived from parameters, we employed standard error propagation methods to determine the uncertainties in the AFM/FM ratio and normalized $A_{\mathrm{FM}}$ and $A_{\mathrm{AF}}$ values.

A selection of fits for both the charge and magnetic scattering signals at different temperatures and field values for M5 and M11 is shown in Fig. 5.

## VI. INTERPARTICLE MAGNETIC ORDERING

Below, we discuss the results of the fit, from which various physical quantities are extracted, including the periodicity and the correlation lengths for the observed charge and magnetic

TABLE II. Overview of the data collected on M5 and M11, where the field values are listed for each temperature. Green and red cells correspond to data for which the lower bound on the 95% confidence interval (CI) for the AFM amplitude (coefficient $c_6$ in the model) was above zero or included zero, respectively. When $c_6$ is zero, the parameters associated with the peak location and width become unidentifiable, and we can make no claims as to their values; therefore, we omit these results.

| | T (K) | H (Oe) | | | | | | | | | |
|---|---|---|---|---|---|---|---|---|---|---|---|
| M5 | 300 | | | | | 200 | 400 | 600 | 1000 | 2000 | 3000 |
| | 15 | | | 0 | | | 400 | 600 | 1000 | 2000 | 3000 |
| M11 | 280 | | | | 100 | 200 | 400 | 600 | 1000 | | 3000 |
| | 20 | −400 | −300 | 0 | 100 | 200 | 400 | 600 | 1000 | | 3000 |

No Data  Lower CI Bound > 0  Lower CI Bound includes 0

correlations as well as their respective strengths and their evolution throughout the magnetization process at various temperatures for both particle sizes.

### A. Data overview and sorting

An overview of the fitted data is shown in Table II, where the field values are listed at each temperature, for M5 and M11. When fitting these data, the parameter relating the AFM correlation length showed unrealistic values for some of the datasets. This typically occurred when no apparent AFM peak was visible in the magnetic scattering signal $R_M$. In Table II, the red cells indicate those datasets for which the lower bound on the 95% confidence interval for the AFM amplitude (coefficient $c_6$ in the model) reached zero, making the estimate of the associated period and correlation length unreliable. The red cells essentially correspond to data collected at high $T$ for M5 and high field values for M11, where no significant AFM component was detected. We chose not to display the fitted AFM period nor the associated correlation lengths for these datasets in the subsequent figures.

### B. Charge and magnetic periodicity

The fitted charge periodicity $p_0$ and magnetic periodicities $p_{FM}$ and $p_{AF}$ are plotted against the applied magnetic field $H$ in Fig. 6.

For both M5 and M11, the fitted charge period $p_0$ remains unchanged when $H$ is varied. When averaged over all field values and all temperatures, the average charge period is $p_0 = 6.29 \pm 0.01$ nm for M5 and $p_0 = 16.5\pm 0.2$ nm for M11. The limited variations (1% or less) across the field range [0, 3000 Oe] confirm that the NPs are not physically moving when a magnetic field up to 3000 Oe is applied. No thermal contraction or dilation of the NP assembly is observed, as the interparticle distance remains unchanged throughout cooling and heating. This suggests that, once the solvent is evaporated after deposition on the silicon nitride membrane, the deposited NPs form a rigid monolayer.

The fitted FM period $p_{FM}$ remains close to the value of the charge period $p_0$ across the entire field range of field values and temperatures. When averaged across magnetic field $H$ and temperature, the average fitted FM period is $p_{FM} = 6.35 \pm 0.13$ nm (a 2% variation) for M5, and $p_{FM} = 16.8 \pm 0.7$ nm (a 4% variation) for M11. The fact that $p_{FM} \approx p_0$ for both the 5 and 11 nm NPs confirms that each NP remains magnetically monodomain throughout magnetizing and throughout cooling/heating.

When the AFM signal is present, the fitted AFM period $p_{AF}$ lands at a value close to $2p_0$. Namely, on average, $p_{AF} = 12.2 \pm 0.4$ nm for M5 and $p_{AF} = 32.5 \pm 3.9$ nm for M11. Here, $p_{AF}$ shows larger variations (up to $\pm 12\%$) across field values than $p_{FM}$. However, the 95% confidence intervals calculated at each $H$ value go up to $\Delta p_{AF} = 1.4$ nm for M5 and up to $\Delta p_{AF} = 15$ nm for M11. This suggests that the observed variations on $p_{AF}$ with $H$ may not reflect a real physical change but are mostly caused by uncertainties on locating the AFM peak due to the wideness of the peak, itself caused by the size inhomogeneities, particularly large for M11. Additionally, the fitted $p_{AF}$ values are spread over a range that includes not only $2p_0$ but other remarkable values such as $\sqrt{3}p_0$, as visible in Fig. 6.

When looking more closely at the fitted values for the AFM peak location over the entire dataset [histogram in Fig. 7(a)], we find that they are distributed around two main values: $q^*/2$ and $q^*/\sqrt{3}$. In real space, this corresponds to periodicities $p_{AF}$ of $2p$ and $\sqrt{3}p$, respectively. Recalling that the XRMS probe is sensitive to the OOP component of the magnetization only, the observed magnetic correlations can only relate to arrangements between OOP nanospins. Given that the studied material consists of 2D monolayers of NPs that tend to form hexagonal lattices, one can associate the two observed $p_{AF}$ values to two distinct AFM arrangements of OOP nanospins within the physical hexagonal lattice of NPs. These magnetic arrangements are illustrated in Fig. 7(b), where the colored dots represent the direction of OOP nanospins and form a magnetic superlattice in the frame of the physical NP hexagonal lattice. One possible arrangement is a linear type, where the nanospin alternation occurs along one direction, as it would be in a 1D chain of NPs. The AFM period in that case is simply twice the nearest-neighbor distance $p_{AF} = 2p_0$. Another arrangement is a honeycomb type [48], where the alternation occurs between nanospins located at the six sites of a hexagon. In that case, the AFM period is the second next-nearest-neighbor distance $p_{AF} = 2\cos(30^\circ)p_0 = \sqrt{3}p_0$. This magnetic honeycomb superlattice arrangement partially addresses the well-known spin-frustration issue that occurs

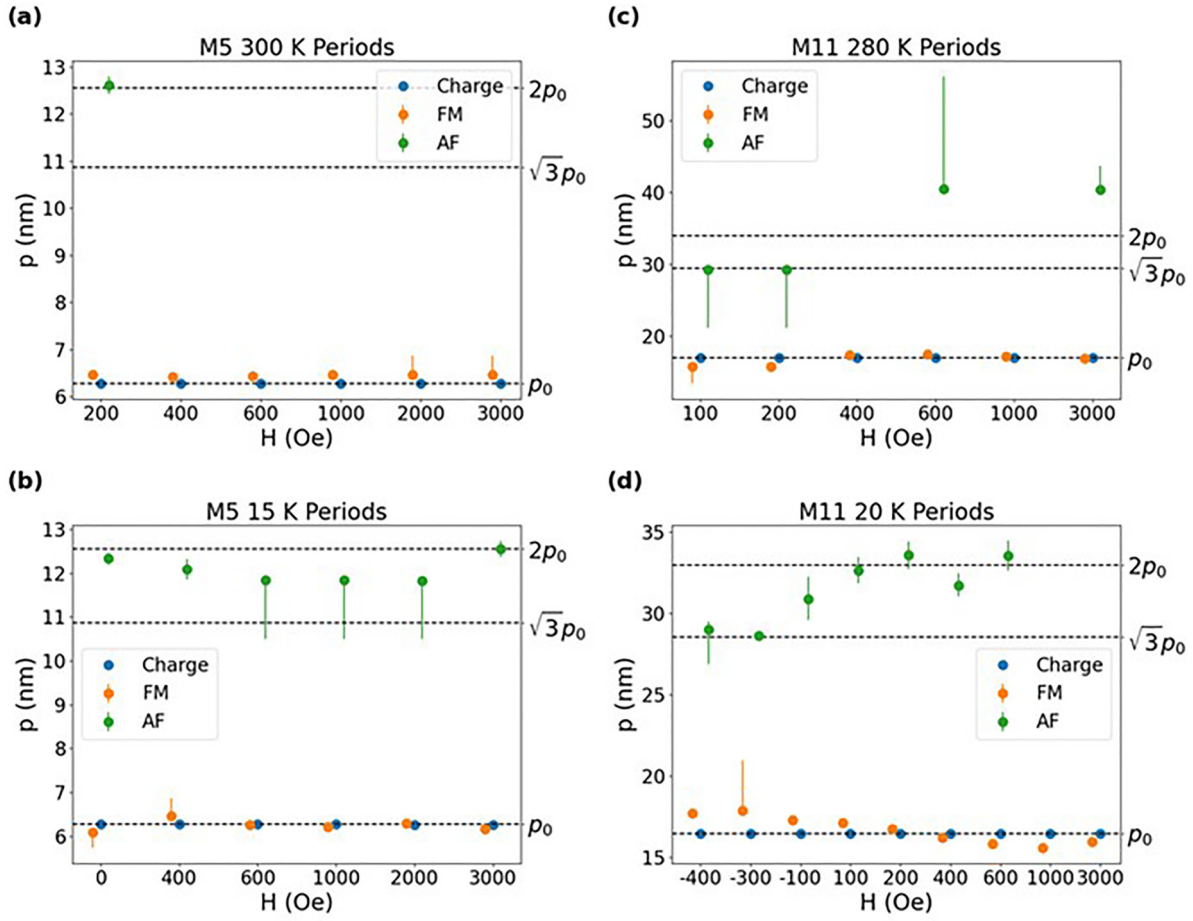


FIG. 6. Periodicities extracted from fitting the charge scattering peak in the $I_0$ signal, as well as the ferromagnetic (FM) and antiferromagnetic (AFM) components in the $R_m$ signal, plotted against the applied magnetic field $H$, for M5 at (a) 300 K and (b) 15 K, and for M11 at (c) 300 K and (d) 20 K. Error bars show the 95% confidence intervals.

for AFM-coupled OOP spins on a triangular (hexagonal) lattice. In the honeycomb superlattice, the six nanospins on the hexagon all satisfy the AFM alternation between OOP neighboring spins. The nanospin situated at the center of the hexagon is represented by an empty circle to signify that its direction is unknown and may as well be oriented in-plane (IP) and not detected via the XRMS probe. While posing a potential spin-frustration issue, the linear AFM arrangement

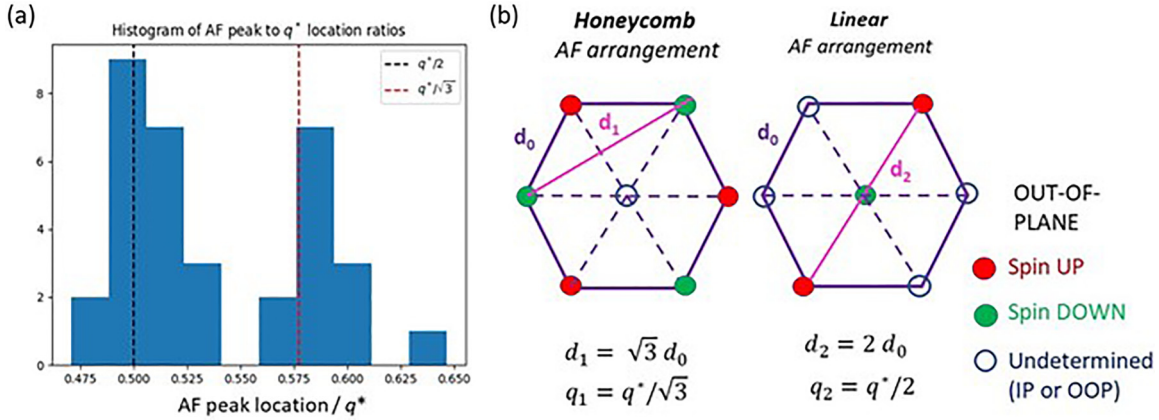


FIG. 7. Visualization of antiferromagnetic (AFM) arrangements of out-of-plane (OOP) nanospins in two dimensions (2D). (a) Histogram of the fitted position $q_{\mathrm{AF}}$ of the AFM component (coefficient $c_7$) for M5 and M11 combined, clearly showing two dominant values, $q^*/2$ and $q^*/\sqrt{3}$. (b) Illustration of possible AFM arrangements of OOP nanospins, in a physical hexagonal lattice of nanoparticles (NPs): a honeycomb lattice of nanospins for the $q^*/\sqrt{3}$ component and a linear arrangement of nanospins for the $q^*/2$ component.

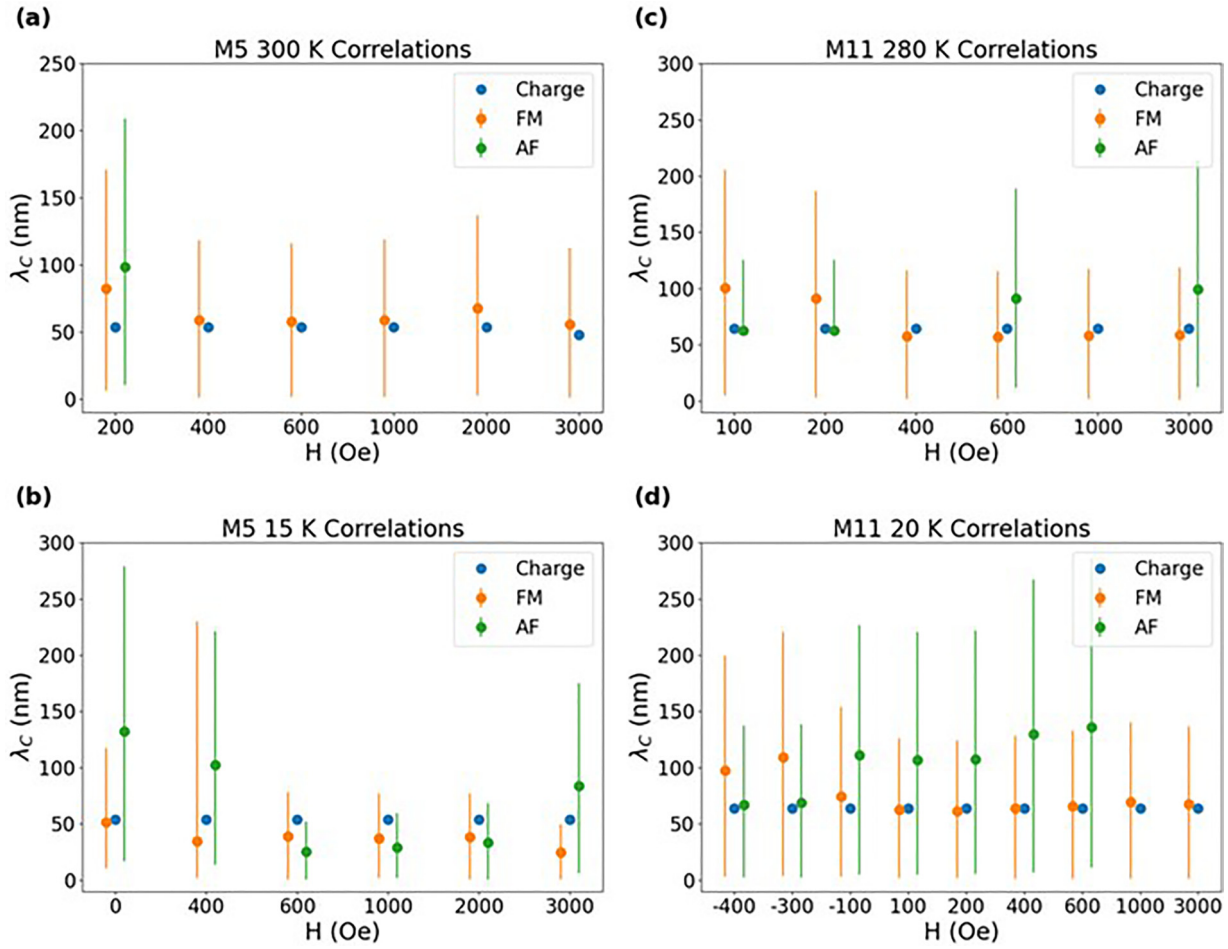


FIG. 8. Correlation lengths extracted from fitting the charge scattering peak in the $I_0$ signal, as well as the ferromagnetic (FM) and antiferromagnetic (AFM) components in the $R_m$ signal, plotted against the applied magnetic field $H$, for M5 at (a) 300 K and (b) 15 K, and for M11 at (c) 300 K and (d) 20 K. Error bars show the 95% confidence intervals.

here id as widely observed as the honeycomb AFM arrangement. Such a variety of magnetic arrangements is possible because of the wide distribution of NP sizes, leading to spatial irregularities in the NP assemblies, composed of sparse islands of hexagonally close-packed NPs, allowing short-ranged 1D chains of NPs to form at locations. On the other hand, some neighboring nanospins may be oriented IP and remain undetected in the XRMS measurement. We note that, while the magnetic dipolar couplings favor the AFM alignment of spins oriented transversally with respect to the direction of the connecting segment (which is the case for OOP nanospins), it also favors the FM alignment of spins oriented colinear with the connecting segment (which would correspond to IP nanospins), thus allowing a wide variety of nanospin arrangements, not all visible via XRMS.

### C. Correlation lengths

The fitted correlation lengths for the respective charge and FM and AFM orderings are shown in Fig. 8. These correlation lengths $\lambda$ are extracted from the fitted peak widths. The correlation length is calculated as follows: When using Gaussian functions, $\lambda = \frac{2\pi}{\sigma}$, and when using Lorentzian function $\lambda = \frac{2\pi}{\omega}\sqrt{2\ln 2}$ to account for the mathematical difference as well as the fact that $I_0$ represents an intensity and $|R_m|$ represents an amplitude.

The fitted charge correlation length, averaged over all field values and temperatures, is found to be $\lambda_c = 64.8 \pm 1.1$ nm for M5, which corresponds to ∼10.3 NPs being correlated in any direction. For M11, $\lambda_c \sim 53.3 \pm 1.6$ nm, which corresponds, on average, to ∼3.2 NPs being correlated in any direction. The values for $\lambda_c$ appear independent of the field magnitude and the temperature. The discrepancy in relative correlation lengths between M5 and M11 is essentially due to particle size inhomogeneity being more pronounced for M11 than M5. The higher homogeneity of 5 nm NPs allows the particles to self-assemble and structurally correlate over longer ranges compared with the more inhomogeneous 11 nm NPs.

The fitted FM correlation length $\lambda_{FM}$ remains relatively stable across field values for both M5 and M11. Like the charge correlations, the FM order appears to extend over a larger number of NPs in the case of the 5 nm NPs than that of 11 nm NPs. For M5, the average FM correlation length at room temperature is $\lambda_{FM} = 60 \pm 12$ nm, which corresponds to ∼9.6 NPs being FM correlated in any direction. For M11, $\lambda_{FM} = 70 \pm 20$ nm, corresponding to ∼4.2 NPs being FM

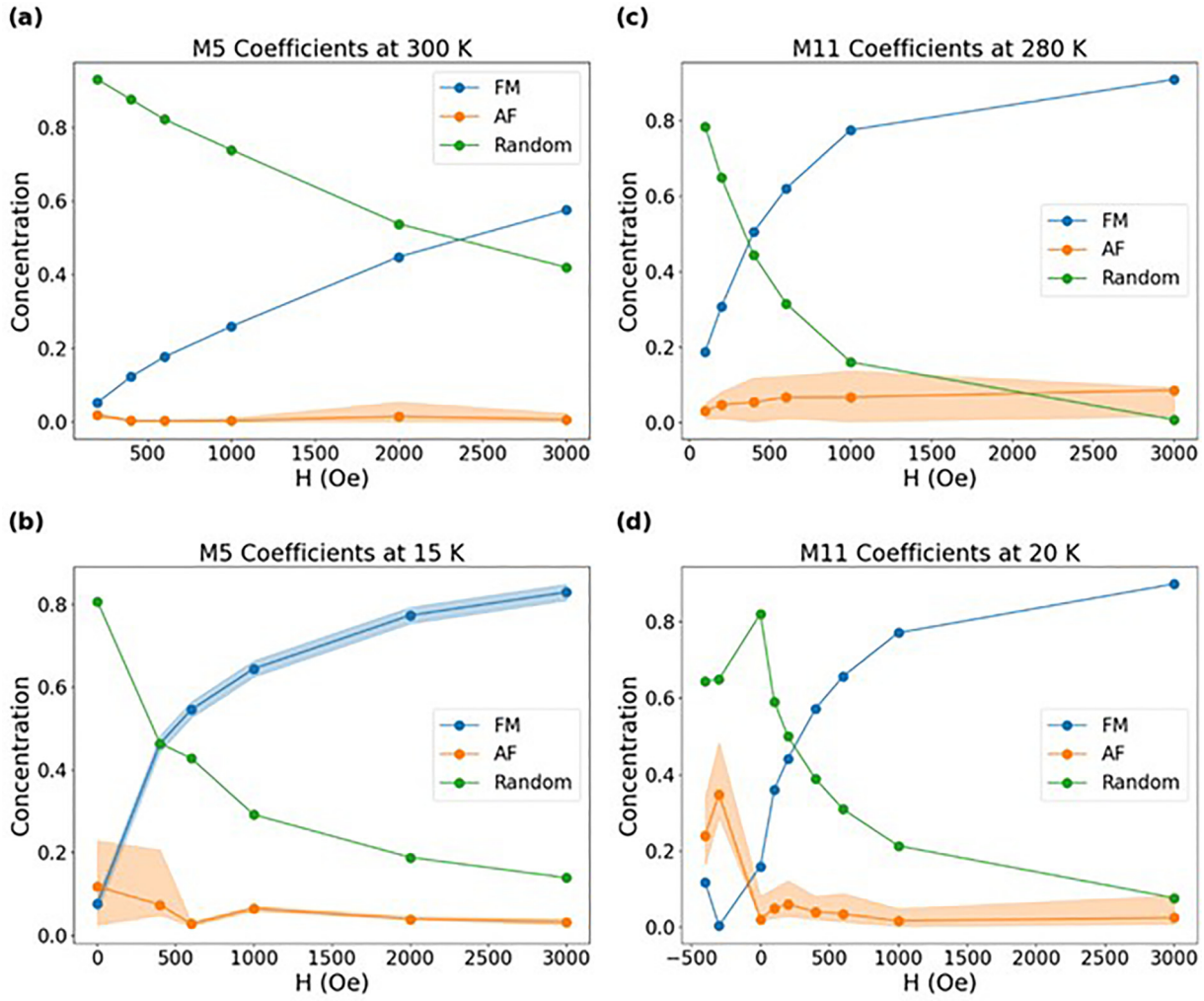


FIG. 9. Concentrations for the ferromagnetic (FM) and antiferromagnetic (AFM) correlations as a function of field $H$, above and below $T_B$, (a) for M5 at 300 K, (b) for M5 at 15 K, (c) for M11 at 280 K, and (d) for M11 at 20 K.

correlated in any direction. These values do not significantly change when cooling down below $T_B$.

The fitted value for $\lambda_{AF}$ shows large (up to 100%) uncertainties at certain field values, so the observed variations of $\lambda_{AF}$ with field $H$ are not meaningful.

### D. Magnetic ordering vs applied magnetic field

The relative amplitudes associated with the fitted FM and AFM components (coefficients $c_3$ and $c_6$ in the model) and their evolution throughout the magnetization process are shown in Fig. 9. For comparison purposes, the FM amplitude $c_{FM}$ is set to the value of the normalized net magnetization $M/M_s$ that was measured via VSM (except near the coercive point where $M = 0$, and instead, the relative magnitude of the magnetic scattering signal $|R_m|$ is used). This normalized concentration $c_{FM}$ is interpreted as the portion of the NP assembly where nanospins align FM OOP. The normalized AFM concentration $c_{AF}$ is accordingly set as $c_{AF} = (c_6/c_3)$ $M/M_s$ and corresponds to the portion of the NP assembly where nanospins align AFM OOP. The sum $c_{FM} + c_{AF}$ should not exceed 1 or 100%. The remaining portion, $1 - c_{FM} - c_{AF}$, corresponds to the portion of the material that is neither FM or AFM correlated OOP and which we identify as magnetic randomness. These random nanospins may be aligned either OOP or IP. The fitted values for these various coefficients for M5 and M11, respectively, are summarized in Table III.

Both M5 and M11 display the following trends at room temperature (above $T_B$): (1) the FM concentration decreases as the field decreases from 3000 Oe to zero according to the respective magnetization curves; (2) the AFM concentration at room temperature remains relatively small (<2.3% for M5 and <9.2% for M11) across all field values; (3) as the field is decreased, the magnetic randomness increases and gradually takes over, reaching up to 93% in the case of M5 and 78% in the case of M11. This confirms the predominant SPM nature of the NP assemblies above $T_B$.

### E. Dependence on temperature

Significant changes in the magnetic behavior are observed when cooling the material from above to below $T_B$. While magnetic randomness remains predominant, a nonnegligeable

TABLE III. Measured and fitted values of selected parameters for M5 and M11, including blocking temperature ($T_B$), coercive field ($H_c$), normalized magnetization ($M/M_s$) at 3000 Oe, fitted periods and correlation lengths for the charge, FM and AFM contributions, fitted concentrations for randomness and AFM order, and fitted AFM/FM concentration ratio.

| | M5 (5 nm) | | M11 (11 nm) | |
|---|---|---|---|---|
| $T_B$ | 28 K | | ∼170 K | |
| Average charge period $p_0$ | $6.29 \pm 0.01$ nm | | $16.5 \pm 0.2$ nm | |
| Average charge correlation $\lambda_c$ | $64.8 \pm 1.1$ nm | | $53.3 \pm 1.6$ nm | |
| Average FM period $p_{\mathrm{FM}}$ | $6.35 \pm 0.13$ nm | | $16.8 \pm 0.7$ nm | |
| Average FM correlation $\lambda_{\mathrm{FM}}$ | $60 \pm 12$ nm | | $70 \pm 20$ nm | |
| Average AFM period $p_{\mathrm{AF}}$ | $12.2 \pm 0.4$ nm | | $32.5 \pm 3.9$ nm | |
| | 300 K | 15 K | 280 K | 20 K |
| $H_c$ | 0 Oe | 0 Oe | 0 Oe | −300 Oe |
| $M/M_s$ @ 3000 Oe | 0.58 | 0.69 | 0.91 | 0.89 |
| Randomness @ 3000 Oe | 42% | 14% | 0.7% | 7.6% |
| Max randomness | 93% | 81% | 78% | 82% |
| Min AFM concentration $A_{\mathrm{AF}}$ | 0.2% | 3.2% | 2.3% | 1.6% |
| Max AFM concentration $A_{\mathrm{AF}}$ | 2.3% | 12% | 9.2% | 35% |
| Max ($A_{\mathrm{AF}}/A_{\mathrm{FM}}$) average ratio | 0.35 | 1.6 | 0.16 | 3.8 |

AFM ordering component emerges at low field values when below $T_B$.

For M5, we observe the following: at 300 K, the randomness concentration starts above 42% at 3000 Oe and increases up to 93% when $H$ is decreased to zero (remanence). Throughout the entire field range, no significant AFM correlations are measured (AFM concentration remains <2.3%). At 15 K below $T_B$, M5 exhibits a similar trend, except the randomness concentration at 3000 Oe is not as high, down to 14%. As the field decreases to zero, the randomness increases up to 81% at remanence, where small but nonnegligeable AFM correlations emerge, covering up to 12%. While the magnetization data for M5 indicates no sign of significant hysteresis at 300 or 15 K, the XRMS data reveal the presence of nonzero AFM correlations between OOP nanospins near remanence. The XRMS data also allow us to quantify the amount of these AFM correlations and see that it sensibly increases (from ∼2 to 10%) when cooling the material below $T_B$.

In the case of M11, AFM correlations between OOP nanospins are also observed, and they appear to be even stronger than for M5. Above $T_B$, the measured AFM concentration reaches up to 9.2% at 300 K. When the material is cooled down to 20 K, below $T_B$ where significant hysteresis is observed ($H_c = 300$ Oe) and when the field is decreased near the coercive point, the AFM concentration significantly increases, covering up to 35% of the NP assembly, with a confidence interval for this parameter ranging from 29% to as high as 48%. Here again, not only the XRMS data corroborate the VSM data which show hysteresis, but they allow us to identify the nature and extent of the magnetic interactions between OOP nanospins at the coercive point.

While discussing temperature dependence, one should account for possible time averaging effects due to the inherent magnetic fluctuation of the nanospins in the NP assemblies. Indeed, in the SPM phase and in the absence of magnetic field, the nanospins supposedly randomly fluctuate at a time scale comparable with or even faster than the measurement time, preventing the observation of any magnetic ordering. However, when cooling the NP assemblies below their blocking temperature, the dynamics of magnetic fluctuation drastically slows down, and at low $T$ well below $T_B$, the nanospin distribution may appear almost static at the timescale of the measurement. It is then possible to observe instantaneous magnetic orderings occurring between the nanospins. In a separate study, we will measure characteristic fluctuation times ranging from ∼200 s at 200 K up to ∼5000 s at 15 K for M5 (for which $T_B \sim 25$ K), and from ∼4000 s at 250 K up to ∼50000 s at 100 K for M11 with $T_B \sim 170$ K). Based on these data, we can comfortably assume that, during the XRMS collection time (∼200 s), the NP assemblies are mostly static, with little effect from magnetic fluctuations on the observed magnetic correlations.

### F. Dependence on particle size

The differences in the magnetic behavior of M5 vs M11 suggest a possible dependence on NP size. To identify a possible trend, we have plotted, in Fig. 10, the relative ratio $c_{\mathrm{AF}}/c_{\mathrm{FM}}$ of the AFM and FM components as a function of $H$. For both M5 and M11, and at all temperatures, this ratio remains relatively small (<0.1) in most of the field range. Only when the field approaches zero (or the coercive point in case hysteresis exists), the AFM/FM ratio starts increasing drastically. At that stage, a noticeable difference is observed between M5 and M11: for M5, the AFM/FM ratio goes up to ∼1.6 with a 95% confidence interval ranging from 0.4 to 3.1, whereas for M11, the AFM/FM ratio goes up to ∼3.8 with a 95% confidence interval ranging from 3.2 to 5.4. This suggests that the NP particle size may affect the strength and extent of AFM correlations when present: The larger 11 nm NPs show a higher AFM concentration than the 5 nm NPs. This effect is likely caused by the drastic increase in the magnitude of the nanospin carried by individual NPs when the NP size increases. In theory, if ignoring surface effects, this increase goes cubically with the particle size. We estimated the nanospin moment for the 5 nm NPs to be $M_n \sim 1400\,\mu_{\mathrm{B}}$, whereas for the 11 nm NPs, $M_n \sim 14000\,\mu_{\mathrm{B}}$, which is ∼10 times stronger. The dipolar magnetic interaction

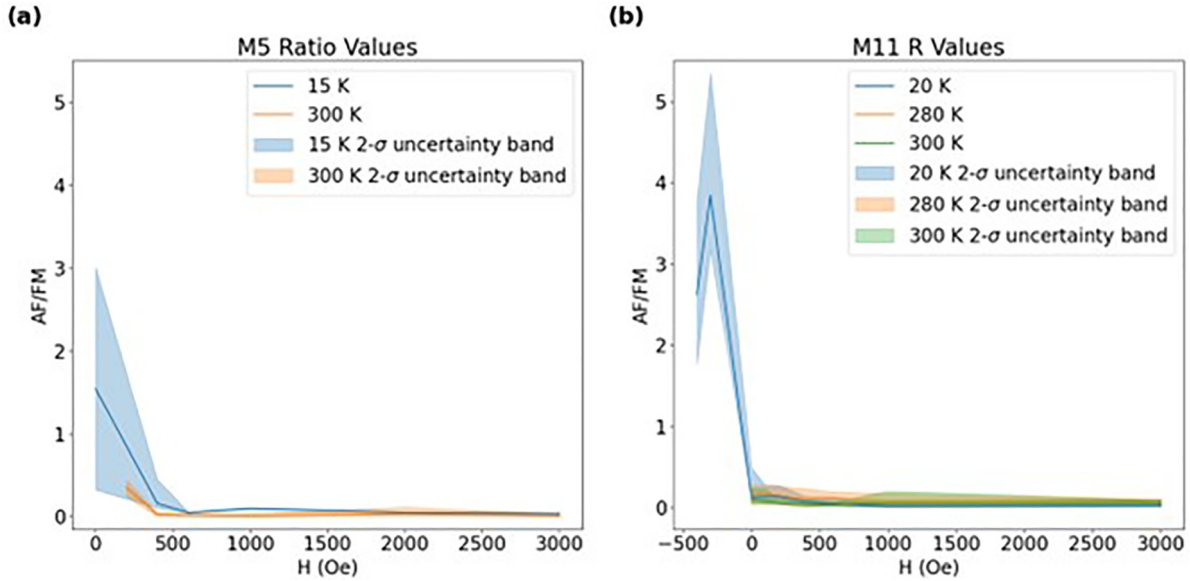


FIG. 10. Relative antiferromagnetic (AFM)/ferromagnetic (FM) ratio vs $H$ field at high and low $T$ for (a) M5 and (b) M11.

between neighboring nanospins, which goes as $E \sim \frac{M_n^2}{p^3}$, increases quadratically with $M_n$. Assuming the interparticle distance $p$ is fixed, this dipolar interaction is amplified by nearly a factor of 100 when increasing the NP size from 5 to 11 nm. The average interparticle distance $p$ also increases from 6.3 to 16.5 nm when going from M5 to M11. However, even when accounting for the larger spacing, the dipolar interaction still increases by about a factor of 5 when going from 5 to 11 nm NPs. Consequently, the AFM correlations are stronger for the larger 11 nm NPs than the 5 nm NPs.

## VII. CONCLUSIONS

Our XRMS study of monolayers of magnetite NPs has unveiled nanoscale interparticle magnetic correlations within 2D assemblies of nanospins that are unseen via other conventional magnetometry techniques and difficult to access via SANS. The XRMS data are particularly instructive when the net magnetization is near zero (which occurs near zero field when in the SPM state or near the coercive point when hysteresis exists), and there is a question whether the nanospins are randomly oriented or magnetically correlated.

If the magnetometry data show no hysteresis, it is generally assumed that, at zero magnetization, the nanospins are magnetically uncorrelated, and magnetic randomness is expected. However, our XRMS data revealed that, even in the absence of visible hysteresis, nanoscale magnetic interparticle correlations between OOP nanospins may exist. Even to a small extent (in the range of a few percent), these correlations, invisible via standard magnetometry, can be detected and quantified via XRMS. If, on the other hand, hysteresis occurs in the magnetization loop, the hysteresis is commonly attributed to various magnetic anisotropies within the NPs, but little is known about the effect of possible interparticle magnetic interactions. The XRMS technique allows us to visualize the nanoscale magnetic correlations at any point of the magnetization loop and thus reveals the nature of the reversal processes through the coercive point. Our XRMS data show that, when applying OOP magnetic field, the hysteresis is accompanied by significant interparticle magnetic correlations and that, at the coercive point, extended AFM ordering occurs between OOP nanospins.

For both the 5 and 11 nm NPs, we found that, when above their respective blocking temperatures $T_B$, magnetic randomness, where the nanospins may be pointing either OOP or IP (nondetected), largely dominates when the magnetic field is released back to zero, confirming the SPM nature of the NP assemblies. However, when these NP assemblies are cooled down below $T_B$, significant OOP interparticle AFM correlations emerge when the magnetic field is released. For the smaller 5 nm NPs, even though no magnetic hysteresis was observed at 15 K, AFM ordering covering up to 12% of the assembly was detected. For the larger 11 nm NPs that exhibit visible hysteresis below $T_B$, more extended AFM correlations covering up to 48% of the assembly were detected at 20 K. These largely extended OOP interparticle magnetic correlations can be physically explained by magnetic dipole couplings, which favor the antiparallel alignment of neighboring dipoles in the direction transverse to the connecting segment.

Based on these findings, useful directions to investigate in the future include further studying the possible role played by interparticle magnetic interactions in the observed hysteresis additional to internal magnetic anisotropies. One way to accomplish this is by varying the average interparticle distance (adjusting the NP concentration) for a given NP size and studying the resulting change in hysteresis and accompanying XRMS signal. It would also be helpful to investigate the dependence on NP size and shape. Additionally, it would be interesting to compare the XRMS signal measured with an *in situ* magnetic field applied IP vs OOP. This may help elucidate the various magnetic contributions to the observed hysteresis and nanospin orderings.

These experimental results may be used to further refine the general modeling of the nanoscale magnetic behavior of

a collection of nanospins, using a combination of Stoner-Wohlfart type of models, with magnetic dipole couplings and Zeeman interaction.

Finally, the XRMS tool can be useful for medical applications, such as hyperthermia, drug delivery, and gene delivery, where functionalized encapsulated magnetic NPs are manipulated via an external magnetic, and their collective response strongly depends on the presence of interparticle magnetic couplings. If interparticle magnetic couplings are undesired in these applications, one could learn to eliminate or control them by adjusting the NP size, structure, and environment. In conclusion, nanoscale magnetic correlations in NP materials are still largely unknown. The XRMS technique allows the detection of interparticle magnetic correlations that cannot be seen via standard magnetometry techniques and provides a way to potentially control and tailor these magnetic correlations for various applications.

## ACKNOWLEDGMENTS

We thank the College of Physical and Mathematical Science at BYU for funding graduate and undergraduate students involved in this research as well as the TEM and VSM instruments. The XRMS data were collected at SSRL at SLAC National Laboratory, supported by the U.S. Department of Energy, Office of Science User Facility.

[1] S. A. Majetich, T. Wen, and R. A. Booth, ACS Nano **5**, 6081 (2011).
[2] S. Mørup, M. F. Hansen, and C. Frandsen, Beilstein J. Nanotechnol. **1**, 182 (2010).
[3] O. Petracic, Superlattices Microstruct. **47**, 569 (2010).
[4] M. Pauly, B. P. Pichon, P. Panissod, S. Fleutot, P. Rodriguez, M. Drillon, and S. Begin-Colin, J. Mater. Chem. **22**, 6343 (2012).
[5] L. M. Wang, A. Qdemat, O. Petracic, E. Kentzinger, U. Rucker, F. Zheng, P. H. Lu, X. K. Wei, R. E. Dunin-Borkowski, and T. Bruckel, Phys. Chem. Chem. Phys. **21**, 6171 (2019).
[6] H. Fang, Z. Yang, C. Ong, Y. Li, and C. Wang, J. Magn. Magn. Mater. **187**, 129 (1998).
[7] S. S. Rao and S. V. Bhat, J. Phys.: Condens. Matter **22**, 116004 (2010).
[8] I. S. Maksymov, Rev. Phys. **1**, 36 (2016).
[9] M. Evangelisti, and E. K. Brechin, Dalton Trans. **39**, 4672 (2010).
[10] M. De, P. S. Ghosh, and V. M. Rotello, Adv. Mater. **20**, 4225 (2008).
[11] N. A. Frey, S. Peng, K. Cheng, and S. Sun, Chem. Soc. Rev. **38**, 2532 (2009).
[12] N. A. Frey and S. Sun, in *Inorganic Nanoparticles: Synthesis, Application, and Perspectives*, edited by C. Altavilla and E. Ciliberto (Taylor and Francis, Milton Park, 2010), Chap. 3, pp. 33–68.
[13] Q. A. Pankhurst, J. Connolly, S. K. Jones, and J. Dobson, J. Phys. D: Appl. Phys. **36**, R167 (2003).
[14] Q. A. Pankhurst, N. T. K. Thanh, S. K. Jones, and J. Dobson, J. Phys. D: Appl. Phys. **42**, 224001 (2009).
[15] Y.-W. Jun, J.-H. Lee, and J. Cheon, Angew. Chem. Int. Ed. **47**, 5122 (2008).
[16] C. C. Berry and A. S. G. Curtis, J. Phys. D: Appl. Phys. **36**, R198 (2003).
[17] R. Hergt, S. Dutz, R. Müller, and M. Zeisberger, J. Phys.: Condens. Matter **18**, S2919 (2006).
[18] H. Markides, M. Rotherham, and A. J. El Haj, J. Nanomater. **2012**, 614094 (2012).
[19] A. C. Doriguetto, N. G. Fernandes, A. I. C. Persiano, E. N. Filho, J. M. Grenèche, and J. D. Fabris, Phys. Chem. Miner. **30**, 249 (2003).
[20] M. Fleet, Acta Cryst. B **37**, 917 (1981).
[21] C. Zener, Phys. Rev. **82**, 403 (1951).
[22] P. W. Anderson and H. Hasegawa, Phys. Rev. **100**, 675 (1955).
[23] M. S. Ansari, M. H. D. Othman, M. O. Ansari, S. Ansari, and H. Abdullah, Appl. Mater. Today **25**, 101181 (2021).
[24] Q. Li, C. W. Kartikowati, S. Horie, T. Ogi, T. Iwaki, and K. Okuyama, Sci. Rep. **7**, 9892 (2017).
[25] G. Cheng, C. L. Dennis, R. D. Shull, and A. R. H. Walker, Cryst. Growth Des. **9**, 3714 (2009).
[26] K. Chesnel, M. Trevino, Y. Cai, J. M. Hancock, S. J. Smith, and R. G. Harrison, J. Phys.: Conf. Ser. **521**, 012004 (2014).
[27] S. Klomp, C. Walker, M. Christiansen, B. Newbold, D. Griner, Y. Cai, P. Minson, J. Farrer, S. Smith, B. J. Campbell *et al.*, IEEE Trans. Magn. **56**, 1 (2020).
[28] G. F. Goya, T. Berquo, F. Fonseca, and M. Morales, J. Appl. Phys. **94**, 3520 (2003).
[29] J. Wang, Q. Chen, X. Li, L. Shi, Z. Peng, and C. Zeng, Chem. Phys. Lett. **390**, 55 (2004).
[30] B. A. Frandsen, C. Read, J. Stevens, C. Walker, M. Christiansen, R. G. Harrison, and K. Chesnel, Phys. Rev. Mater. **5**, 054411 (2021).
[31] J. L. Dormann, D. Fiorani, and E. Tronc, in *Advances in Chemical Physics*, edited by I. Prigogine and S. A. Rice (John Wiley & Sons, Hoboken, 1997), Vol. 98.
[32] S. Morup and E. Tronc, Phys. Rev. Lett. **72**, 3278 (1994).
[33] V. F. Puntes, P. Gorostiza, D. M. Aruguete, N. G. Bastus, and A. P. Alivisatos, Nat. Mater. **3**, 263 (2004).
[34] Y. Cai, K. Chesnel, M. Trevino, A. Westover, R. Harrison, J. Hancock, S. Turley, A. Scherz, A. Reid, B. Wu *et al.*, J. Appl. Phys. **115**, 17B537 (2014).
[35] D. Mishra, O. Petracic, A. Devishvili, K. Theis-Bröhl, B. P. Toperverg, and H. Zabel, J. Phys.: Condens. Matter **27**, 136001 (2015).
[36] K. Krycka, R. Booth, J. Borchers, W. Chen, C. Conlon, T. Gentile, C. Hogg, Y. Ijiri, M. Laver, B. Maranville *et al.*, Physica B **404**, 2561 (2009).
[37] D. Honecker, M. Bersweiler, S. Erokhin, D. Berkov, K. Chesnel, D. A. Venero, A. Qdemat, S. Disch, J. Jochum, A. Michels *et al.*, Nanoscale Adv. **4**, 1026 (2022).
[38] Y. Yamamoto, T. Miura, M. Suzuki, N. Kawamura, H. Miyagawa, T. Nakamura, K. Kobayashi, T. Teranishi, and H. Hori, Phys. Rev. Lett. **93**, 116801 (2004).

[39] J. Kortright, D. Awschalom, J. Stöhr, S. Bader, Y. Idzerda, S. Parkin, I. K. Schuller, and H.-C. Siegmann, J. Magn. Magn. Mater. **207**, 7 (1999).
[40] K. Chesnel, D. Griner, D. Smith, Y. Cai, M. Trevino, B. Newbold, T. Wang, T. Liu, E. Jal, A. H. Reid *et al.*, Magnetochemistry **4**, 1026 (2018).
[41] J. Rackham, B. Newbold, S. Kotter, D. Smith, D. Griner, R. Harrison, A. H. Reid, M. Transtrum, and K. Chesnel, AIP Adv. **9**, 035033 (2019).
[42] J. B. Kortright, O. Hellwig, K. Chesnel, S. Sun, and E. E. Fullerton, Phys. Rev. B **71**, 012402 (2005).
[43] S. Sun and H. Zeng, J. Am. Chem. Soc. **124**, 8204 (2002).
[44] C. Altavilla, E. Ciliberto, D. Gatteschi, and C. Sangregorio, Adv. Mater. **17**, 1084 (2005).
[45] N. R. Jana, Y. Chen, and X. Peng, Chem. Mater. **16**, 3931 (2004).
[46] M. Newville, T. Stensitzki, D. B. Allen, M. Rawlik, A. Ingargiola, and A. Nelson, Astrophysics Source Code Library, ascl:1606.014 (2016).
[47] M. Blume, J. Appl. Phys. **57**, 3615 (1985).
[48] R. F. Bishop, P. H. Y. Li, D. J. J. Farnell, and C. E. Campbell, J. Phys.: Condens. Matter. **24**, 236002 (2012).

# Chapter 3

# Ptychography Imaging

This chapter constitutes the basis for a manuscript with the working title of

"Direct magnetic imaging of superparamagnetic nanoparticles via resonant x-ray dichroic ptychography"

and authors list:

Johnathon Rackham[1], Taylor Buckway[1], Alex Ditter[2], David Shapiro[2], Arentxa Rodriquez[3], Adriana Figueroas[3], Richard L. Sandberg[1], and Karine Chesnel[1].

1. Physics Department, Brigham Young University
2. Advanced Light Source, Stanford
3. University of Barcelona, Spain

My contributions to this work include the collection of the data, its processing for the dichroic analysis, and the writing of this manuscript.

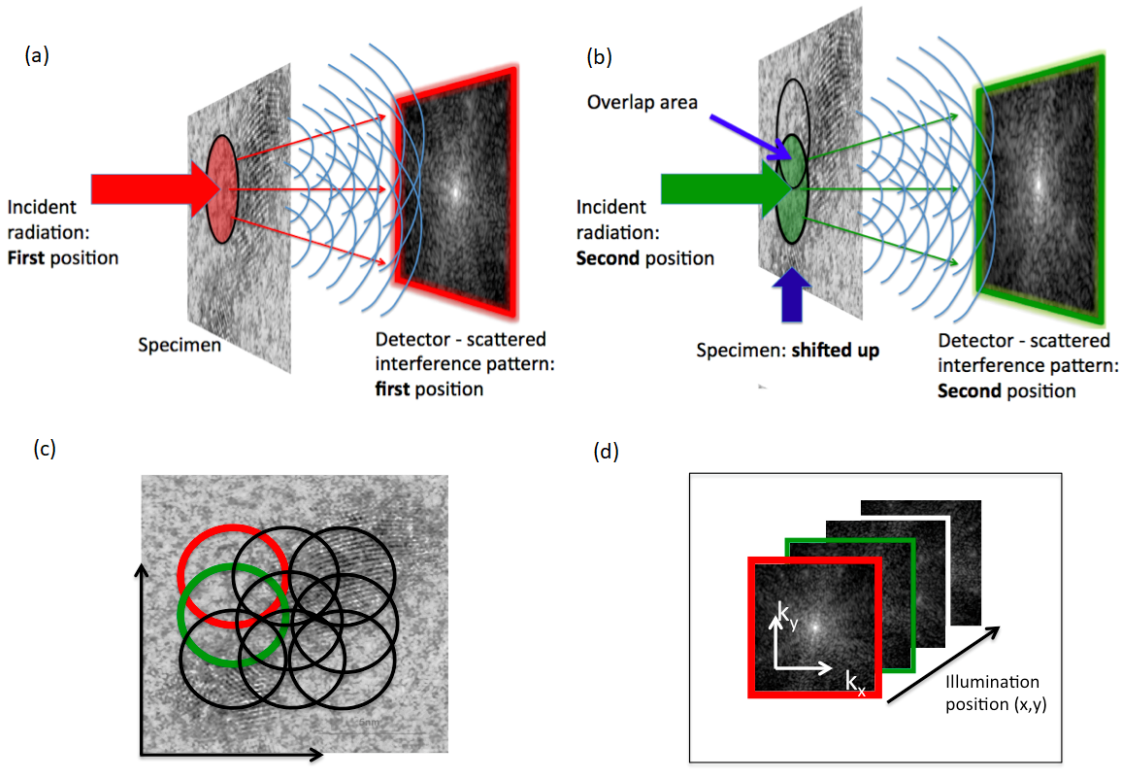


**Figure 3.1** A collection of a ptychographic imaging data set. (a) Coherent illumination incident from the left is locally confined onto an area of the sample. A detector downstream of the sample records a diffraction pattern. (b) The sample is shifted (in this case, upwards) and a second pattern is recorded. Note that regions of illumination must overlap with one another to facilitate robust phase retrieval. (c) A whole ptychographic data set uses many overlapping regions of illumination. (d) for each 2D illumination position (x, y), there is a 2D diffraction pattern (kx, ky) [14].

## 3.1 Introduction

The results presented in the previous chapter are based on scattering signals produced by millions of NPs illuminated together by x-rays. These methods offer great value in extracting broad statistical information about the properties of NP assemblies, but do not provide a direct view of the local magnetic ordering. Ptychography provides a way to extract localized real-space images that we can examine to probe local magnetic ordering.

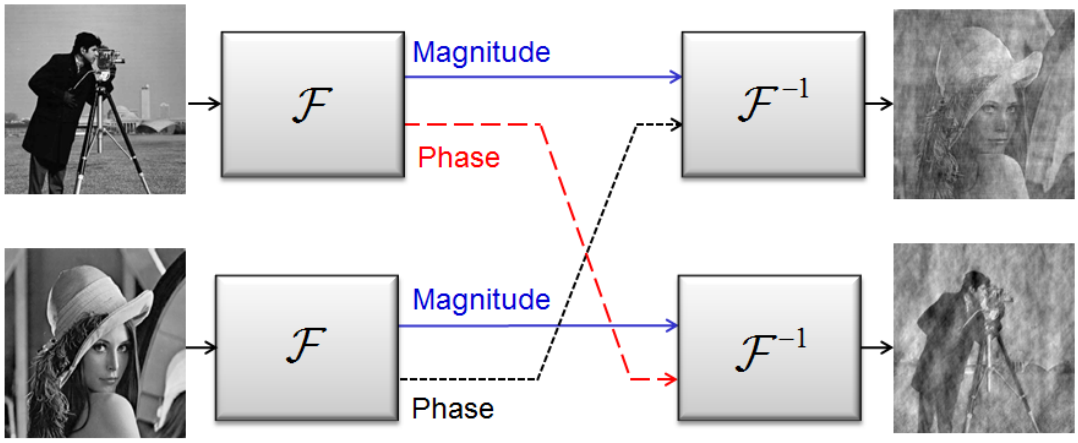


**Figure 3.2** A synthetic example demonstrating the importance of Fourier phase in reconstructing a signal from its Fourier transform (courtesy of [16, 17]).

Ptychography is a computational imaging technique that reconstructs images of samples by processing overlapping diffraction patterns collected as a coherent probe scans across an object (as shown in Fig. 3.1). The overlap between adjacent illuminated regions provides redundant information which is essential for a robust and unambiguous phase retrieval process. This process computationally reconstructs both the amplitude and phase of the sample's exit surface wave [15]. Fig. 3.2 illustrates how significant the phase is to a resultant image by taking the phase of one image and swapping it with the phase of the other, we can see that almost all of the structural information about an image is contained in the phase [16].

Although modern ptychography emerged in the 21st century, its conceptual roots trace back to the 1960s and 1970s in electron microscopy and crystal structure determination [18]. Iterative algorithms for ptychography, such as the ePIE (extended Ptychographical Iterative Engine), significantly accelerated practical reconstructions and enabled widespread adoption in diverse imaging contexts [19,20]. It is fundamentally a lensless imaging method with a broad range of applications, especially in X-ray science, electron microscopy, and optical microscopy [21].

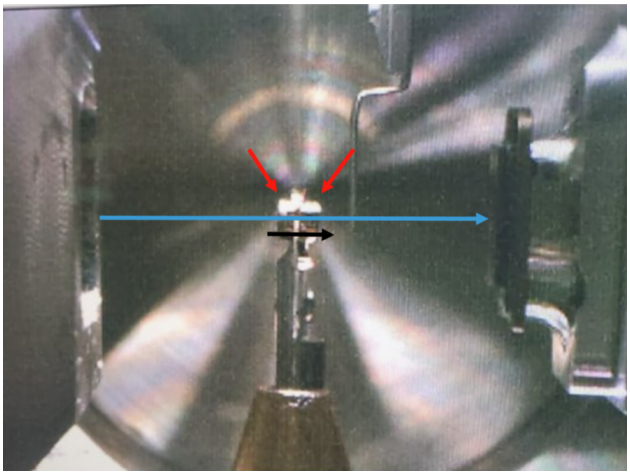

**Figure 3.3** Mounting of two rare earth magnets (indicated by red arrows) on the tip of the sample holder to provide an *in situ* magnetic field for XAS and XMCD analysis. Red arrows indicate the magnets, blue the direction of incident x-rays, and black the direction of the applied magnetic field.

Advances in ptychography methods have enabled resolution in the nanoscale, making probing NP behavior more accessible [22, 23]. By exploiting the dichroism present in magnetic NPs, we can resolve the magnetic texture of NP assemblies and better characterize the local behavior of these particles for their many uses and applications [24]. This work utilizes ptychography to provide a real-space picture of the magnetic ordering in our NP samples.

## 3.2 Stage Preparation

The magnetite NPs we use in this study were synethized in an organic chemical solution at BYU by Dr. Roger Harrison, and at the University of Barcelona by Dr. Arentxa Rodriquez, and Dr. Adriana Figueroas according to the methods described in their respective papers [10, 25]. In this work we examine ptychographic reconstructions of three samples with average particle sizes of approximately 18 nm, 45nm, and 68 nm diameters. The NPs were deposited on TEM membranes

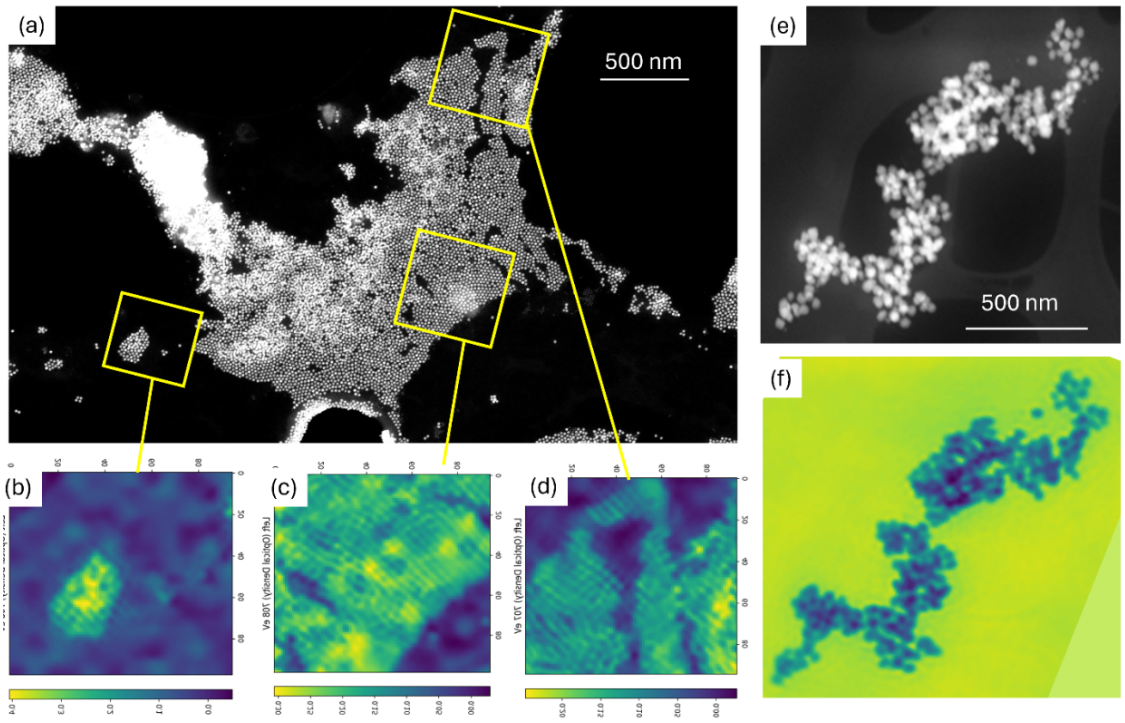


**Figure 3.4** TEM images (collected at BYU) and x-ray ptychographic reconstructions (obtained at COSMIC, ALS with 708 eV x-rays) of same regions of Fe3O4 nanoparticle samples. (a) TEM image of a North America shaped vast monolayer region made of 18 nm closed packed NPs (b-c) ptychographic reconstructions of various sub-regions: (b) Hawaii, (c) Texas, (d) Quebec; (e) TEM image of an island made of 45 nm NPs; (f) ptychographic reconstruction of the exact same region.

via a drop casting method with care to ensure the membranes were not overly saturated with NPs and enabled to form islands of mono-layer regions.

In order to tune the illuminating x-rays to the proper resonant energy, we first carried out XAS spectroscpy measurements to show XMCD in order to identify the relevant absorption edges. These measurements require a way to expose the sample to an *in situ* magnetic field. We accomplished this by mounting two small toroidal shaped rare earth magnets on either side of the sample wafer to provide an out-of-plane magnetic field of about 500 Oe in magnitude. The mounting structure is shown in Fig. 3.3

## 3.3 X-ray Energy Tuning

To optimize the magneto-optical contrast in the scattering signal, the energy of the illuminating radiation needs to be tuned to a resonance edge. This study uses the $L_3$ edge of iron where the greatest spin-orbit couplings occur in the Fe atoms. For magnetite $Fe_3O_4$, the XMCD signal is expected to exhibit three sub-peaks corresponding to the octahedral and tetrahedral sites for the Fe ions in the crystal structure and these three peaks have alternating signs in the XMCD signal. We expect the magnetic scattering signals to alternate in sign as well when the energy is tuned to these three peaks. If the sign of the signal in the dichroic ptychography reconstruction does switch sign when changing the energy, it proves the magnetic nature of the dichroic image. Fig. 3.5 shows the reconstructed x-ray absorption spectra (XAS) based on integrating STXM images collected over the energy range [690-730 eV] of the sampled magnetite NPs and the dichroism that arises from the opposite polarities of the illuminating x-rays. We successfully observed the three peaks in the XMCD spectrum and as we move in energy across the peaks, we observed a sign change at the middle of the three peaks.

## 3.4 Ptychographic Reconstruction and Dichroism

The ptychographic reconstructions were performed at the ALS using an automatic differentiation based algorithm [26] to retrieve the phase, specifically the CDtools python library documented here [27]. This method reconstructs the the exit surface wave and is represented in computation as a complex valued $(a+bi)$ array. Using this resultant array we can calculate two quantities. First, the optical density

$$OD = -ln(A/A_0)$$

with $A$ being the amplitude calculated

$$A = \sqrt{a^2+b^2}$$

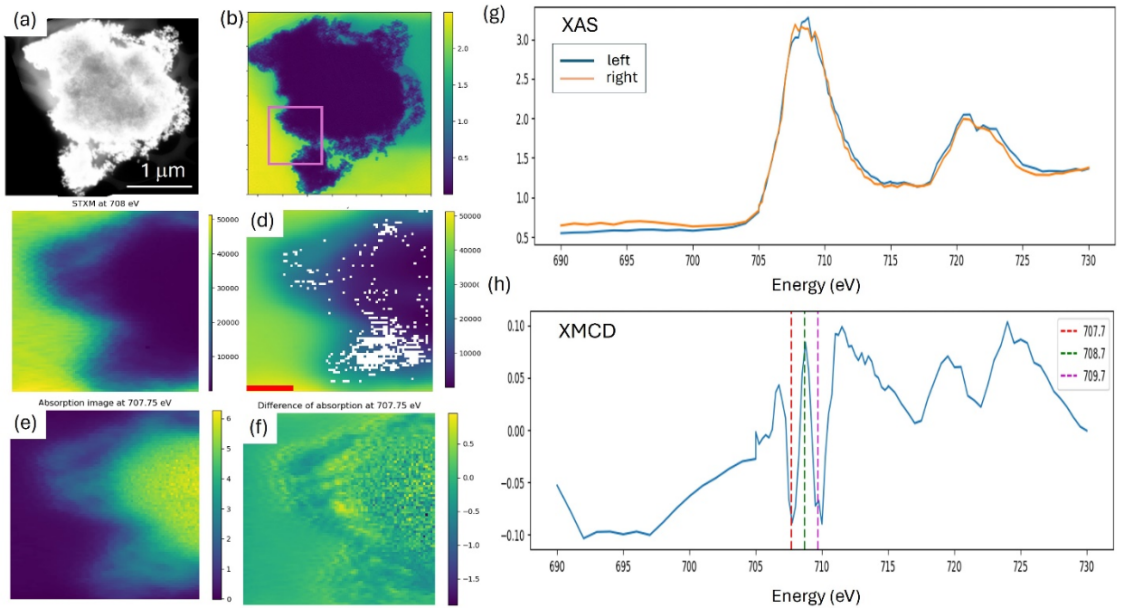


**Figure 3.5** XAS and XMCD spectra extracted from STXM images under a magnetic field H of ∼500 Oe (a) TEM image of the region studied: a compact cluster of 45 nm NPs. (b) x-ray ptychographic reconstructions of the exact same region (c) STXM image of the sub-region highlighted by the pink square shown in (a); (d) visualization of the pixels used for the integrating the signal (in white) and of the region used for I0 (red line) to compute the (e) absorption image and (f) dichroic STXM image. (b-f) all collected at the L3-Fe resonance near 708 eV. (g) integrated XAS signal; (h) resulting smoothed XMCD signal over 690-730 eV range.

and $A_0$ being the average amplitude of a subregion of the image containing no material for normalizing out any fluctuations in illuminating intensity. Second, we can also examine the phase of the reconstruction image.

$$\phi = arctan(b/a)$$

Because we have reconstructed images from opposite polarities of illuminating x-rays we can examine the contrast between them in both dichroic optical density

$$OD_{dichroic} = OD_L - OD_R$$

and differential phase

$$\phi_{diff} = \phi_L - \phi_R$$

to isolate the magnetic texture and therefore infer the local magnetic ordering present in the samples. Found within Appendix A is a proof showing how magnetic information can be retrieved from diffraction data.

## 3.5 Results

Our approach demonstrates a viable way of using ptychographic methods to provide imaging of the local magnetic ordering found in magnetite NPs. The magnetic ordering we see exhibits behavior consistent with the XMCD spectrum in that it switches sign as we move the energy of the illuminating x-rays through the absorption peaks shown in Fig. 3.6a. If we examine one of the circled particles in panel (d) and follow it through the changes in energy (panels e, and f) we can see the particle's phase change sign just like what is predicted by the XMCD spectrum.

Additionally, we can observe an ordering that matches measurable statistics and which is predicted by the modeling methods described above [28]. Slice (a) through the image shown in Fig. 3.7 reveals a sequence of NPs that are aligned in an anti-ferromagnetic order, while slice (b) indicates

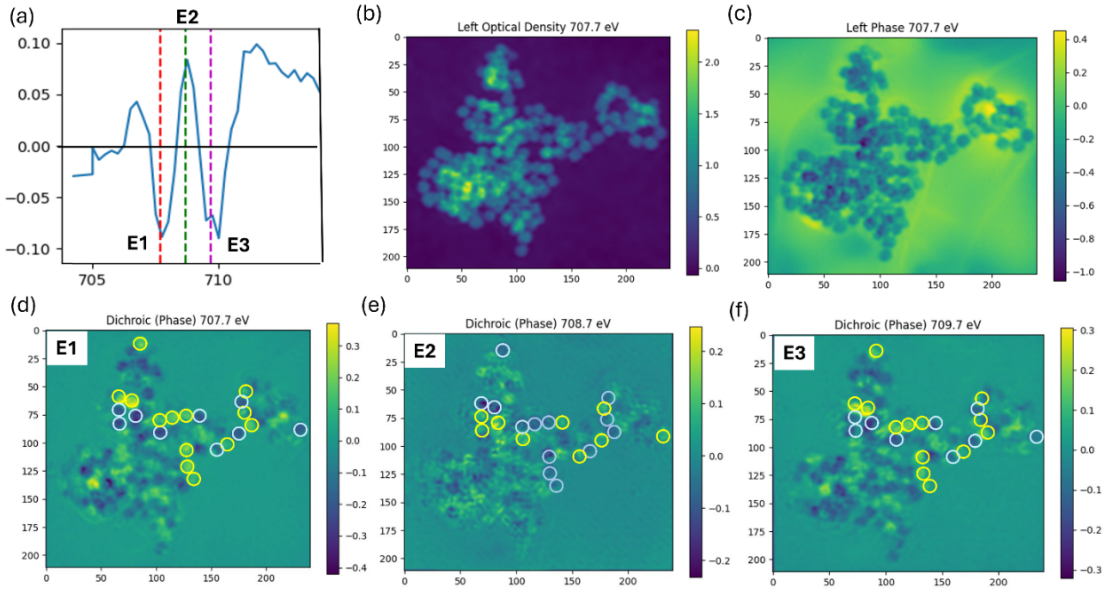


**Figure 3.6** Illustration of pure magnetic contrast on an assembly of 68 nm NPs. (a) Zoomed-in view of the XMCD signal showing three resonances at E1=707.7 eV, E2= 708.7 eV and E3 = 709.7 eV; (b) Reconstructed absorption signal at E1; (c) Reconstructed phase at E1; (d-f) Dichroic phase at (d) E1, (e) E2, (f) E3.

a cluster of particles that are ferromagnetically aligned with one another. The magnetic ordering we observe is predominantly ferromagnetic ordering, but has small portions of antiferromagnetic ordering that remains correlated out to approximately three to four particle diameters, exactly as our correlation modeling predicts. Taking these observations into account, we can conclude that the textures we see in the differential phase images are magnetic in nature.

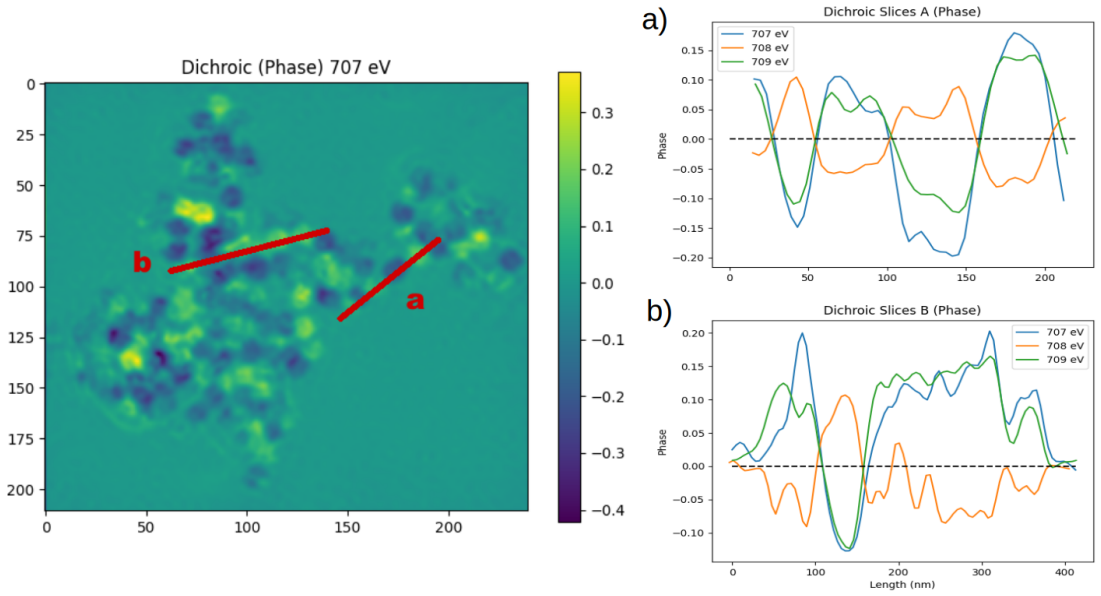


**Figure 3.7** (left) Illustration of pure magnetic contrast for assembly of 68 nm NPs. (a) slice of the phase contrast shown on the left along indicated line indicating anti-ferromagnetic ordering. (b) Another slice through the phase contrast showing a more ferromagnetic configuration of NPs.

# Chapter 4

# Dynamics of Magnetic Fluctuations

This chapter constitutes the basis for a manuscript with the working title of

"Dynamics of magnetic fluctuations in superparamagnetic nanoparticle assemblies probed via coherent x-ray correlation spectroscopy"

and authors list:

Johnathon Rackham[1], Corey Hawkins[1], Nathon Woolley[1], Claudio Mazzoli[2], Arentxa Rodriquez[3], Adriana Figueroas[3], and Karine Chesnel[1].

1. Physics Department, Brigham Young University
2. National Synchrotron Light Source II, New York
3. University of Barcelona, Spain

My contributions to this work include the collection of the data at NSLS-II, its analysis for the XPCS study described below, and the writing of this manuscript.

## 4.1 Introduction

The results discussed previously assume static magnetic systems, but in reality the magnetic configurations in our samples are dynamic. Understanding these dynamics is crucial for functionalizing nanoparticle assemblies for their technological applications. Investigating the dynamic magnetic behavior of magnetite nanoparticles requires tools capable of resolving both structural and magnetic fluctuations on nanometer length scales and relevant timescales. Although techniques like photothermal magnetic circular dichroism have recently enabled the study of magnetization switching in individual 20 nm magnetite particles [29], x-ray photon correlation spectroscopy (XPCS) offers a complementary approach to characterize collective nanoparticle dynamics in situ.

XPCS is a powerful technique for probing nanoscale dynamics in condensed matter systems, with applications extending to complex fluids, soft matter, and nanoparticles [30, 31]. The method exploits the coherence of synchrotron or free-electron laser x-ray sources to measure temporal fluctuations in scattered intensity, providing insight into slow dynamic processes on microsecond to second timescales [32, 33]. Recent advances, such as nanofocused beams, have enhanced XPCS sensitivity and resolution, enabling the study of nanoscale structural and magnetic fluctuations with unprecedented detail [32, 34].

Here, we present an X-ray photon correlation spectroscopy study of magnetite nanoparticles of various sizes throughout the superparamagnetic transition. This work aims to resolve nanoscale fluctuations in magnetite nanoparticles, contributing to a deeper understanding of their dynamic magnetic behavior with implications for both fundamental science and technological applications [29, 32, 34].

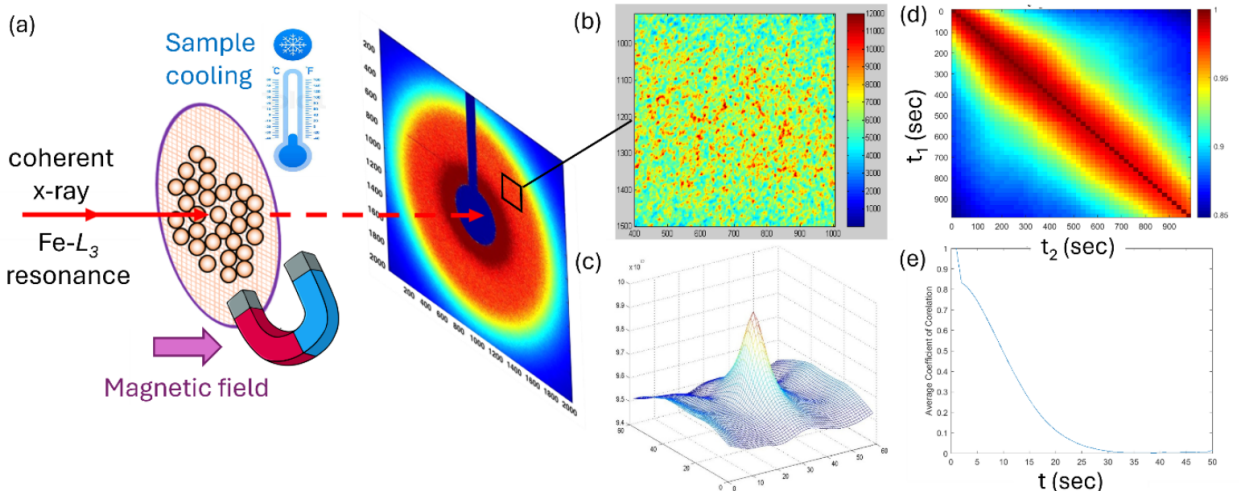


**Figure 4.1** Illustration of our XPCS measurements on MNPs and data processing. (a) Experimental setup for the XPCS measurement where monolayers of Fe3O4 NPs with in-situ cooling and magnetic field are illuminated in transmission geometry by coherent x-rays tuned to the Fe-L3 edge and a scattering pattern is collected on a CCD downstream; (b) Zoomed-view on a collected scattering pattern showing speckles; (c) Cross-correlation pattern between a pair of speckle patterns; (d) Two-time correlation map, where each pixel represents the correlation degree between two speckle images collected at times t1 and t2. (d) One-time correlation curve resulting from integrating the two-time map diagonally at given time laps.

## 4.2 Setup and Sample

We focus here on two samples of magnetite nanoparticles to conduct our XPCS study, a 5 nm sample manufactured at BYU as discussed in the previous chapters as well as a 18 nm provided by our collaborators at the University of Barcelona; Dr. Arantxa Rodriguez, and Dr. Adriana Figueroas. The 5 nm sample is made up of a closed-packed monolayer as seen later in Fig. 4.2a while the TEM imaging of the 18 nm sample, shown in Fig. 4.4a suggests the nanoparticles are forming sparser island monolayers. The speckle patterns for the XPCS study for these 5 nm and 18 nm samples were collected at the NSLS-II and SOLEIL synchrotrons respectively.

## 4.3 Methods of Correlation

XPCS relies on the cross-correlation of a time series of coherent speckle patterns. As discussed above these speckle patterns constitute a unique fingerprint of the magnetic ordering present in the sample. Cross-correlating a time series of these patterns allows us to extract how the magnetic configurations change in time. The conventional method of correlation uses the $g_2$ function

$$g_2(q,t') = \frac{< I(q,t)(q,t+t') >}{< I(q,t) >^2}$$

where $I(q,t)$ refers to the scattering intensity at the momentum vector $q$ in reciprocal space at time $t$ and the $< \cdots >$ refer to averages over time $t$. The quantity $t'$ is the delay time. This work uses an implementation of this method in the python library scikit-beam. The method is detailed more in the published work of Lumma *et al.* [35], and the code documented here [36].

Additionally, we make use of a novel correlation method that can be used to better account for many experimental errors and thermal drift that the sample might experience over the course of the time series by doing a full spatial correlation of the speckle patters and integrating under the peak (example peak shown in Fig. 4.1c)

$$\rho = \frac{\sum C_{a,b}}{\sqrt{\sum C_{a,a} \sum C_{b,b}}}$$

where $C$ refers to the cross-correlations operation between images (a,b, ...) and the $\sum$ symbol represents the integration over the correlation signal. Here we use a small circular area around the correlation peak as the area of integration in order to fully capture the correlation signal, but exclude the sub-peaks related to correlation with neighboring speckles. In both correlation methods, any multiplication of intensities is pixel-wise and we generate two-time maps of the time correlation as illustrated in Fig. 4.1d.

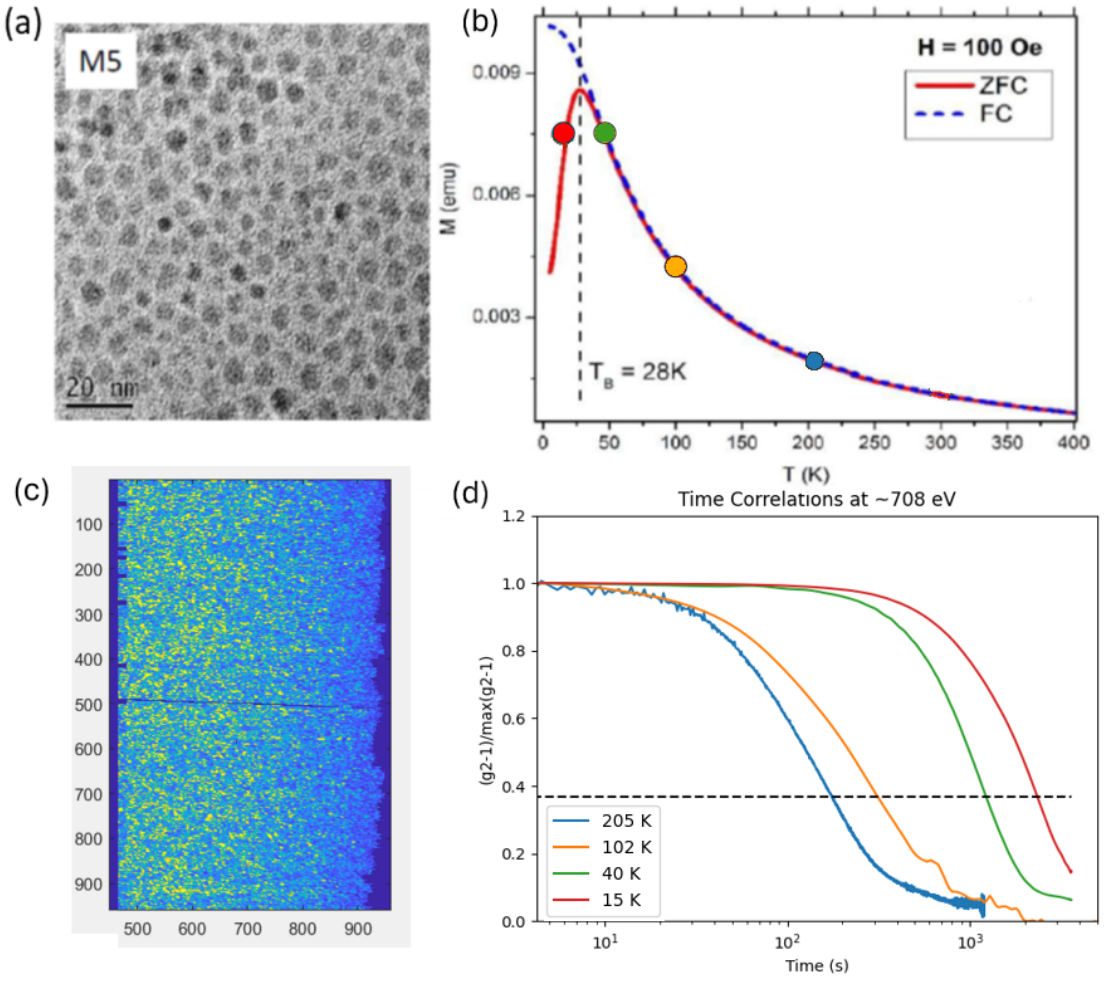


**Figure 4.2** Results on 5 nm NPs (a) TEM image showing a monolayer of closed packed NPs; (b) Field cooling (FC/ ZFC) curves collected under 100 Oe, indicating a blocking temperature TB = 28 K; (c) speckle pattern collected at the Fe-L3 edge at NSLSII; (d) Normalized time-correlation curves measured at T = 15 K, 40 K, 102 K and 205 K

## 4.4 Results

Fig. 4.2 details the results of the XPCS study we carried out at the NSLS-II beamline. Panel b features the FC/ZFC curve associated with our sample with points indicating the temperatures at which we collected the time series. We examined the behavior of these particles at two temperatures (15 K, and 40 K) near the blocking temperature, $T_B = 28$K, and two additional temperatures (102 K, and 205 K) well above $T_B = 28$K. Across this temperature range, we observe an inverse relationship between the characteristic fluctuation time and temperature. As the sample cools, the timescale of the dynamics of magnetic fluctuations lengthens with a noticeable jump below the blocking temperature where spin moments of the particles become progressively blocked from flipping. Fig. 4.3 details a plot of the characteristic times as a function of temperature. Here we see the clear decay in the rate of fluctuation as temperatures change with the timescales spanning an order of magnitude ranging from approximately 130 s to 1900 s.

Additionally we show preliminary results for the 18 nm sample with data collected at SOLEIL. Figure 4.4 shows the two-time map and correlation signals for these NPs. Fig. 4.5 details the characteristic fluctuation time results so far as being between approximately 150 s and 1600 s. We expect these times to be longer for 18 nm compared to 5 nm. We have other data on 11 nm NPs that supports a similar superparamagnetic transition but has much greater values ($10^3$ to $10^4$ sec) than the 5 nm particles. The characteristic fluctuation times for the 18 nm NPs should be even greater than the 11 nm NPs.

At the time of writing, we believe this discrepancy to be due to several potential factors. We believe that there may have been issues related to the cooling of the sample and not giving sufficient time to allow for the stresses induced by cooling the sample to stabilize. Additionally, this data was collected using a CMOS detector that has periodic damage at spatial frequencies that may be relevant to the correlations because of the sporadic, island nature of the sample. We are currently investigating ways to mitigate these issues and this is a topic for further study.

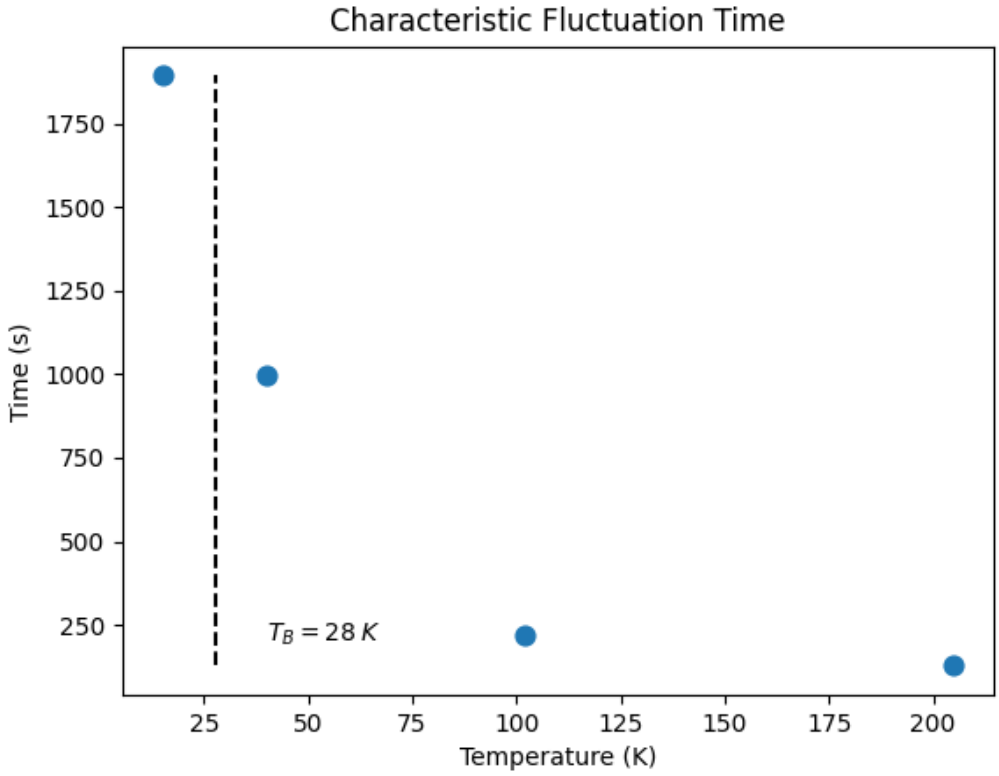


**Figure 4.3** Map of the characteristic times for 5 nm NPs as a function of temperature showing the overall trend in the dynamics of fluctuations showing a significant increase in time scales as we decrease temperature, particularly below the blocking temperature ($T_B$ = 28 K)

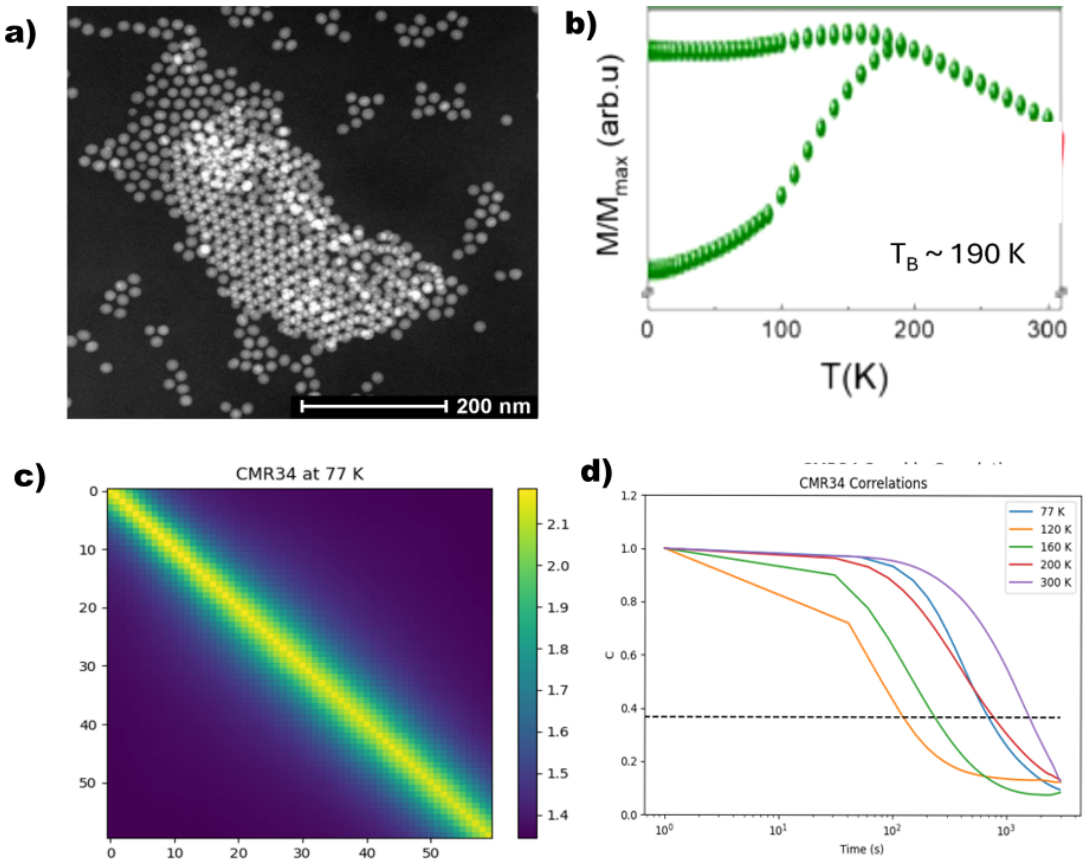


**Figure 4.4** Preliminary results on 18 nm NPs (a) TEM image showing a monolayer island of closed packed NPs; (b) Field cooling (FC/ ZFC) curves collected under 100 Oe, indicating a blocking temperature TB = 190 K; (c) two-time correlation map for the CMR34 sample using speckle patterns collected at SOLEIL; (d) Normalized time-correlation curves measured at T = 77 K, 120 K, 160 K, 200 K, and 300 K.

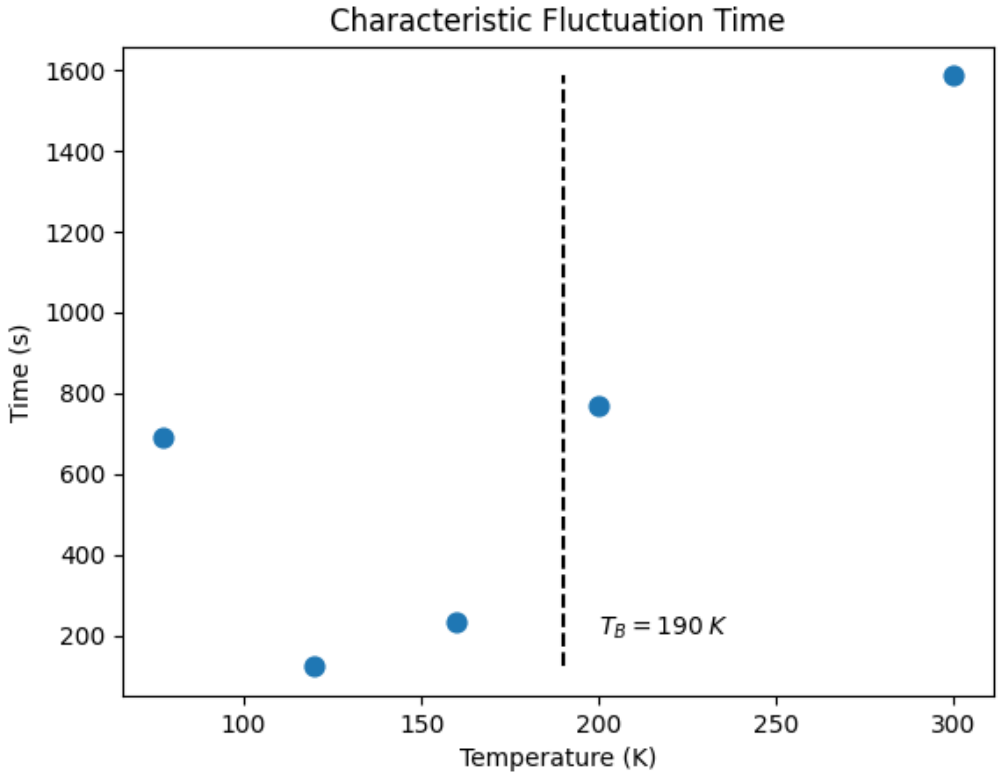


**Figure 4.5** Preliminary map of the characteristic times for 18 nm NPs as a function of temperature showing the overall trend in the dynamics of fluctuations for NPs with ($T_B$ = 190 K)

# Chapter 5

# Conclusion

In this work, we have established the viability of computational modeling techniques to characterize the inter-particle magnetic correlations in assemblies of magnetic NPs using XRMS data. Our modeling of the NP assemblies at temperatures above and below their respective blocking temperatures ($T_B$) shows that when the applied field ($H$) approaches remanence, the nanospin carried by the individual NPs tends to be randomly oriented though a non-negliable AF contribution is present in the samples at temperatures below the blocking temperature. This behavior is consistent across both the real space nanochain and empirical q-space fitting models and confirms the superparamagnetic behavior of the material at $T > T_B$. Additionally, it appears that the AF correlations are stronger for the larger NPs compared to the smaller ones with the former's AF/FM ratio 3 times larger.

The dichroic ptychography methods we use produce real space images that can be validated as containing magnetic texture. The texture observed in the dichoric images has behavior consistent with the expected sign flipping as we move through the energies of the XMCD spectra. Furthermore, the dichroic images indicate that when magnetite nanoparticles form simple monolayer structures, they can form antiferromagnetic ordering. The ordering observed in the images has correlation lengths corresponding to several particle diameters, as predicted by our modeling methods.

Our XPCS methods have quantified the characteristic time scales for 5 nm nanoparticles as ranging from 130 s to 1900 s when the sample moves in temperature from below the blocking temperature to approaching room temperature. These observations are congruent with expected behavior, and while the results for the 18 nm particles are not fully realized and inconclusive, the scale of their characteristic times are of similar but different magnitudes. This points to the potential dependency of particle size on the characteristic time of nanoparticle dynamics of magnetic fluctuations.

While this work provides much needed insight into the nanoscale behavior of magnetite nanoparticles, there are still many ways the research can be built upon and expanded. First, regarding the magnetic correlation modeling, we have additional data collected at the SOLEIL beamline which comprises a set of data through both the ascending and descending branches of the magnetization loops. Analyzing this data would allow us to map the AF and FM components of the NP assemblies throughout the full magnetization loop. This additional data also features samples where the nanoparticles are more dispersed on the TEM membranes, which we could examine in order to determine the effects particle density and interparticle distance might have on the magnetic orders present in the sample.

Second, the results of the dichroic ptychography study can be improved. The Coherent Diffraction Imaging lab at BYU, headed up by Dr. Richard Sandberg, has made great progress in developing in-house capabilities to perform ptychographic reconstructions. It is possible that the initial results provided by the ALS team can be improved upon, specifically the reconstructions of the smaller NPs, to achieve better resolution. With improved resolution we could also begin examining the time series data we collected and piece together a real-space movie of the changing magnetic configuration. Additionally, one of the challenges of ptychography is the non-linear warping of the image that can occur through the reconstruction process. A robust way of handling diffeomorphic

image registration to better align images for dichroic analysis would be instrumental for further research.

Finally, we can expand upon the XPCS study through the post-processing of the SOLEIL dataset to potentially resolve the discrepancies in the results. Further work has also been done on more NP sizes and these results could be folded into a comparative study on how particle size affects the dynamics of magnetic fluctuations. Additionally, we could perform an analytical study comparing and contrasting the two correlation methods we used in this work.

The x-ray based methods we have utilized in this work have enabled us to successfully probe the nanoscale behavior of magnetite nanoparticles. Here, we provide a baseline characterization of magnetic configurations and their dynamics of fluctuation in assemblies of various sizes, and while these results are only part of the comprehensive whole, they can serve as the basis for new research. We invite any future collaboration to further our understanding of magnetic nanoparticles.

# Appendix A

# Dichroism and Magnetic Ratio Derivation

X-ray magnetic circular dichroism proves to be an effective tool at extracting the magnetic signal from scattering data. To do this, we use the theory of magnetic scattering where the scattering factor $f$ may be written as

$$f_{\pm} = f_c \pm f_m$$

with $f_c$ and $f_m$ are the charge and magnetic scattering factors respectively with $\pm$ representing the helicity of the circularly polarized light in the plane transverse to propagation.

The scattering amplitude $A$ of a nanoparticle assembly in a given direction $q$ in the scattering space can then be expressed as

$$A_{\pm}(q) = \sum (f_{c,j} \pm f_{m,j}) e^{i\vec{q}\cdot\vec{r}j} = f_c s_c \pm f_m s_m = A_c \pm A_m$$

where the summation indexed by $j$ is over all the atoms. We simplify the expression for the $A$ by introducing a charge and magnetic structure factor, $s_c$ and $s_m$. These both respectively depend on the spatial distributions of the charge and magnetism in the sample, and are both $q$ dependent. The scattering amplitude $A$ can therefore be written as a sum of the charge and magnetic amplitudes

$A_c$ and $A_m$. The scattering intensity $I$ observed at the detector is related to the scattering amplitude through

$$I_{\pm} = |A_{\pm}|^2 = |A_c|^2 \pm (A_c A_m^* + A_m A_c^*) + |A_m|^2$$

The scattering intensity is comprised of a pure charge term, $|A_c|^2$, a pure magnetic term, $|A_m|^2$, and a cross term whose sign is dependent on the polarization of incident light. We can exploit the difference polarization has on the scattering to extract the magnetic contribution using a quantity we call "magnetic ratio $R_m$" (modified from the standard dichroic ratio)

$$R_m = \frac{I_+ - I_-}{\sqrt{I_+ + I_-}}$$

Where $I_+$ and $I_-$ are the intensities associated with their respective helicities. The magnetic component $A_m$ is typically small with respect to $A_c$ which reduces the dichroic ratio to:

$$R_m = \frac{A_c A_m^* + A_m A_c^*}{\sqrt{|A_c|^2 + |A_m|^2}} \sim \frac{A_c A_m^* + A_m A_c^*}{|A_c|}$$

The numerator can be further reduced but breaking the complex quantities $A_c$ and $A_m$ into their real and imaginary components.

$$f_c = f_{c,1} + i f_{c,2} \text{ and } f_m = f_{m,1} + i f_{m,2}$$

$$s_c = s_{c,1} + i s_{c,2} \text{ and } s_m = s_{m,1} + i s_{m,2}$$

The results of the x-ray absorption spectroscopy (XAS) collected on the magnetite nanoparticles shows that at the energy chosen for our XRMS measurements (the third peak of our observed $L_3$-Fe

absorption edge), the real part of the magnetic scattering factor tends to vanish. Therefore, we assume that $f_{m,1} \sim 0$ in order to give $A_c$ and $A_m$ the following form

$$A_c = (f_{c,1} + if_{c,2})(s_{c,1} + is_{c,2}) = (f_{c,1}s_{c,1} - f_{c,2}s_{c,2}) + i(f_{c,2}s_{c,1} + f_{c,1}s_{c,2})$$
$$A_c^* = (f_{c,1}s_{c,1} - f_{c,2}s_{c,2}) + i(f_{c,2}s_{c,1} + f_{c,1}s_{c,2})$$
$$A_m = (f_{m,1} + if_{m,2})(s_{m,1} + is_{m,2}) = (f_{m,1}s_{m,1} - f_{m,2}s_{m,2}) + i(f_{m,2}s_{m,1} + f_{m,1}s_{m,2})$$
$$A_m^* = (f_{m,1}s_{c,1} - f_{m,2}s_{c,2}) + i(f_{m,2}s_{c,1} + f_{m,1}s_{m,2})$$

which leads to

$$\begin{aligned} A_c A_m^* &= -if_{m,2}(s_{m,1} - is_{m,2})[(f_{c,1}s_{c,1} - f_{c,2}s_{c,2}) + i(f_{c,1}s_{c,2} + f_{c,1}s_{c,2})] \\ &= [-f_{m,2}s_{m,2}(f_{c,1}s_{c,1} - f_{c,2}s_{c,2}) + f_{m,2}s_{m,1}(f_{c,2}s_{c,1} + f_{c,1}s_{c,2})] \\ &+ i[-f_{m,2}s_{m,1}(f_{c,1}s_{c,1} - f_{c,2}s_{c,2}) - f_{m,2}s_{m,1}(f_{c,2}s_{c,1} + f_{c,1}s_{c,2})] \end{aligned}$$

and

$$A_c A_m^* + A_m A_c^* = 2Re(A_c A_m^*) = 2[-f_{m,2}s_{m,2}(f_{c,1}s_{c,1} - f_{c,2}s_{c,2}) + f_{m,2}s_{m,1}(f_{c,2}s_{c,1} + f_{c,1}s_{c,2})]$$

resulting in

$$R_m \approx \frac{2f_{m,2}[s_{m,1}(f_{c,2}s_{c,1} + f_{c,1}s_{c,2}) - s_{m,2}(f_{c,1}s_{c,1} + f_{c,2}s_{c,2})}{|f_c||s_c|}$$

The coefficients $f_{c,1}$, $f_{c,2}$ and $f_m$ are estimated with the XAS data using Kramer-Kronig transformations. $s_{c,1}$, $s_{c,2}$, $s_{m,1}$, $s_{m,2}$ are calculated with the Fourier transforms that are part of our model for the charge density function, and magnetic density functions in a chain of $Fe_3O_4$ NPs. All these quantities depend on the scattering vector $q$, so $R_m$ does as well. In the end the modeled $R_m(q)$ and the experimental $R_m(q)$ are compared and various parameters in the model are adjusted to make the model match the experiment. In this process, the quantities $s_{c,1}$, $s_{c,2}$ (and the resulting $|s_c|$) are

concurrently evaluated by fitting the experimental charge scattering intensity:

$$(I_+ + I_-)(q) = |A_c|^2 + |A_m|^2 \approx |A_c|^2 = |f_c|^2 |s_c|^2$$

Once the charge structural factors $s_{c,1}$, and $s_{c,2}$ are adjusted, the magnetic structural factors $s_{m,1}$, and $s_{m,2}$ are adjusted by fitting $R_m(q)$. A weight for the various magnetic components (FM, AF, and random) is then evaluated as well as their respective correlation lengths.

*Derivation courtesy of Dr. Karine Chesnel, and published in part in* [13]

# Bibliography


[1] N. A. Frey, S. Peng, K. Cheng, and S. Sun, "Magnetic nanoparticles: synthesis, functionalization, and applications in bioimaging and magnetic energy storage," Chem. Soc. Rev. **38,** 2532–2542 (2009).

[2] S. Mornet, S. Vasseur, F. Grasset, and E. Duguet, "Magnetic nanoparticle design for medical diagnosis and therapy," J. Mater. Chem. **14,** 2161–2175 (2004).

[3] E. Duguet, S. Vasseur, S. Mornet, and J.-M. Devoisselle, "Magnetic nanoparticles and their applications in medicine," Future Medicine (2006).

[4] J. Gao, H. Gu, and B. Xu, "Multifunctional magnetic nanoparticles: design, synthesis, and biomedical applications," Accounts of chemical research **42,** 1097–1107 (2009).

[5] D. P. Thomsen HS, Morcos SK, Clin Radiol. 61 (11): 905–6. doi:10.1016/j.crad.2006.09.003. PMID 17018301 (2006).

[6] A. Ito, M. Shinkai, H. Honda, and T. Kobayashi, "Medical application of functionalized magnetic nanoparticles," Journal of bioscience and bioengineering **100,** 1–11 (2005).

[7] N. Sezer, İbrahim Arı, Y. Biçer, and M. Koç, "Superparamagnetic nanoarchitectures: Multimodal functionalities and applications," Journal of Magnetism and Magnetic Materials **538,** 168300 (2021).

[8] E. Verwey, "Electronic conduction of magnetite (Fe3O4) and its transition point at low temperatures," Nature **144,** 327–328 (1939).

[9] M. Fleet, "The structure of magnetite," Acta Crystallographica Section B: Structural Crystallography and Crystal Chemistry **37,** 917–920 (1981).

[10] K. Chesnel, M. Trevino, Y. Cai, J. M. Hancock, S. J. Smith, and R. G. Harrison, "Particle size effects on the magnetic behaviour of 5 to 11 nm Fe3O4 nanoparticles coated with oleic acid," Journal of Physics: Conference Series **521,** 012004 (2014).

[11] S. Klomp *et al.*, "Size-Dependent Crystalline and Magnetic Properties of 5–100 nm Fe3O4 Nanoparticles: Superparamagnetism, Verwey Transition, and FeO–Fe3O4 Core–Shell Formation," IEEE Transactions on Magnetics **56,** 1–9 (2020).

[12] Y. Cai *et al.*, "Orbital and spin moments of 5 to 11 nm Fe3O4 nanoparticles measured via x-ray magnetic circular dichroism," Journal of Applied Physics **115,** 17B537 (2014).

[13] K. Chesnel *et al.*, "Unraveling Nanoscale Magnetic Ordering in Fe3O4 Nanoparticle Assemblies via X-rays," Magnetochemistry 4 (2018).

[14] Wikipedia, "Ptychography — Wikipedia, The Free Encyclopedia,", http://en.wikipedia.org/w/index.php?title=Ptychography&oldid=1304626258, 2025, [Online; accessed 07-August-2025].

[15] F. Pfeiffer, "X-ray ptychography," Nature Photonics (2018).

[16] K. Jaganathan, Y. C. Eldar, and B. Hassibi, "Phase retrieval: An overview of recent developments," Optical compressive imaging pp. 279–312 (2016).

[17] Y. Shechtman, Y. C. Eldar, O. Cohen, H. N. Chapman, J. Miao, and M. Segev, "Phase retrieval with application to optical imaging: a contemporary overview," IEEE signal processing magazine **32,** 87–109 (2015).

[18] J. M. Rodenburg, "Ptychography: early history and 3D scattering effects," In *Short-Wavelength Imaging and Spectroscopy*, D. Bleiner, ed., pp. 867809–867809–10 (2012).

[19] A. M. Maiden and J. M. Rodenburg, "An improved ptychographical phase retrieval algorithm for diffractive imaging.," Ultramicroscopy **109,** 1256–62 (2009).

[20] A. Maiden, D. Johnson, and P. Li, "Further improvements to the ptychographical iterative engine," Optica **4,** 736–745 (2017).

[21] J. M. Rodenburg, A. C. Hurst, A. G. Cullis, B. R. Dobson, F. Pfeiffer, O. Bunk, C. David, K. Jefimovs, and I. Johnson, "Hard-X-Ray Lensless Imaging of Extended Objects," Physical Review Letters **98,** 34801 (2007), copyright (C) 2010 The American Physical SocietyPlease report any problems to prola@aps.orgPRL.

[22] F. Pfeiffer, "X-ray ptychography," Nature Photonics **12,** 9–17 (2018).

[23] J. M. Rodenburg, "Ptychography and related diffractive imaging methods," Advances in imaging and electron physics **150,** 87–184 (2008).

[24] Y. H. Lo *et al.*, "X-ray linear dichroic ptychography," Proceedings of the National Academy of Sciences of the United States of America 118 (2021).

[25] C. Moya *et al.*, "Unveiling the crystal and magnetic texture of iron oxide nanoflowers," Nanoscale **16,** 1942–1951 (2024).

[26] S. Kandel, S. Maddali, M. Allain, S. O. Hruszkewycz, C. Jacobsen, and Y. S. Nashed, "Using automatic differentiation as a general framework for ptychographic reconstruction," Optics express **27,** 18653–18672 (2019).

[27] A. Levitan, *CDTools: a python library for ptychography and CDI reconstructions.*, 2024, v0.3.0pypi1.

[28] J. Rackham, B. Pratt, D. Griner, D. Smith, Y. Cai, R. G. Harrison, A. Reid, J. Kortright, M. K. Transtrum, and K. Chesnel, "Field-dependent nanospin ordering in monolayers of Fe 3 O 4 nanoparticles throughout the superparamagnetic blocking transition," Physical Review B **108,** 104415 (2023).

[29] S. Adhikari, Y. Wang, P. Spaeth, F. Scalerandi, W. Albrecht, J. Liu, and M. Orrit, "Magnetization switching of single magnetite nanoparticles monitored optically," Nano Letters **24,** 9861–9867 (2024).

[30] O. G. Shpyrko, "X-ray photon correlation spectroscopy," Synchrotron Radiation **21,** 1057–1064 (2014).

[31] G. Grübel, A. Madsen, and A. Robert, "X-ray photon correlation spectroscopy (XPCS)," in *Soft Matter Characterization* (Springer, 2008), pp. 953–995.

[32] S. Berkowicz *et al.*, "Nanofocused x-ray photon correlation spectroscopy," Physical Review Research **4,** L032012 (2022).

[33] W. Roseker *et al.*, "Towards ultrafast dynamics with split-pulse X-ray photon correlation spectroscopy at free electron laser sources," Nature communications **9,** 1704 (2018).

[34] C. Klose, F. Büttner, W. Hu, C. Mazzoli, G. S. Beach, S. Eisebitt, and B. Pfau, "Photon correlation spectroscopy with heterodyne mixing based on soft x-ray magnetic circular dichroism," Physical Review B **105,** 214425 (2022).

[35] D. Lumma, L. Lurio, S. Mochrie, and M. Sutton, "Area detector based photon correlation in the regime of short data batches: Data reduction for dynamic x-ray scattering," Review of Scientific Instruments **71,** 3274–3289 (2000).

[36] *Scikit-beam correlation module.*, 2024.